Article

Cell Reports

PRMT1 Is Recruited via DNA-PK to Chromatin Where It Sustains the Senescence-Associated Secretory Phenotype in Response to Cisplatin

Graphical Abstract

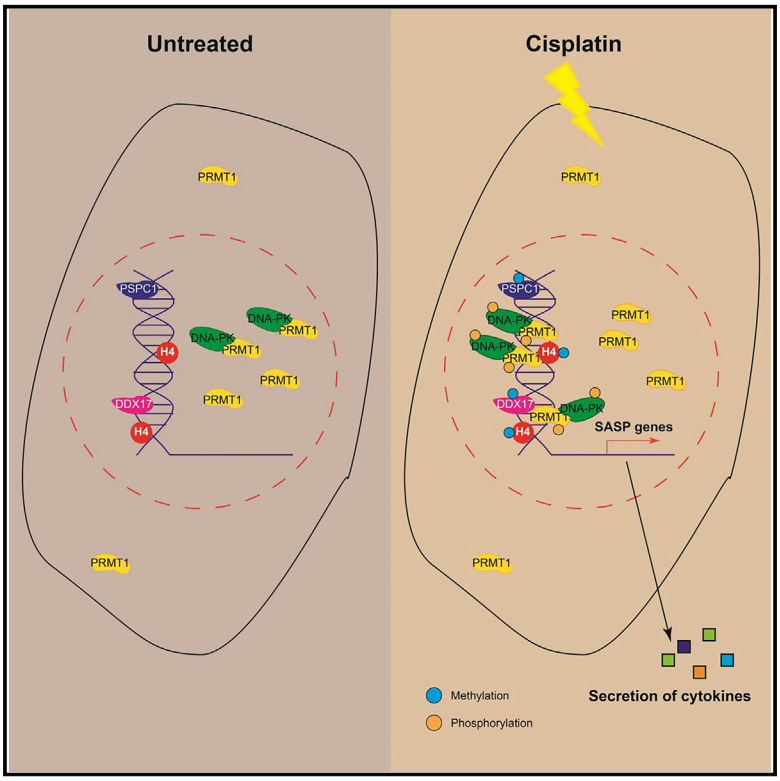

Authors

Daniele Musiani, Roberto Giambruno, Enrico Massignani, ..., Luciano Nicosia, Diego Pasini, Tiziana Bonaldi

Correspondence

tiziana.bonaldi@ieo.it

In Brief

Protein arginine methyltransferase 1 (PRMT1) overexpression is linked to cancer chemoresistance, but the mechanism is still unclear. Musiani et al. show that, upon cisplatin, PRMT1 is recruited by DNA-dependent protein kinase (DNA-PK) to chromatin, where it sustains the transcription of genes involved in the senescence-associated secretory phenotype (SASP), thus protecting cells from drug-induced apoptosis.

Highlights

- Cisplatin leads to increased PRMT1 association to chromatin and H4R3 methylation
- PRMT1 increase in chromatin is mediated by DNA-PK
- Chromatin-associated PRMT1 sustains the transcription of SASP genes
- Inhibition or genetic depletion of PRMT1 blocks SASP and sensitizes cancer cells to cisplatin

Musiani et al., 2020, Cell Reports *30*, 1208–1222
January 28, 2020 © 2019 The Author(s).
https://doi.org/10.1016/j.celrep.2019.12.061

CellPress

OPEN ACCESS
CellPress

Cell Reports
Article

PRMT1 Is Recruited via DNA-PK to Chromatin Where It Sustains the Senescence-Associated Secretory Phenotype in Response to Cisplatin

Daniele Musiani,[1,3,5] Roberto Giambruno,[1,5] Enrico Massignani,[1] Marica Rosaria Ippolito,[1] Marianna Maniaci,[1] Sriganesh Jammula,[1,4] Daria Manganaro,[1] Alessandro Cuomo,[1] Luciano Nicosia,[1] Diego Pasini,[1,2] and Tiziana Bonaldi[1,6,*]
[1]Department of Experimental Oncology, IEO, European Institute of Oncology IRCCS, Milan 20139, Italy
[2]Department of Health Sciences, University of Milan, Milan, Italy
[3]Present address: Inserm U830, PSL Research University, Institut Curie, 75005 Paris, France
[4]Present address: Cancer Research UK Cambridge Institute, Cambridge, UK
[5]These authors contributed equally
[6]Lead Contact
*Correspondence: tiziana.bonaldi@ieo.it
https://doi.org/10.1016/j.celrep.2019.12.061

SUMMARY

Protein arginine methyltransferase 1 (PRMT1) is overexpressed in various human cancers and linked to poor response to chemotherapy. Various PRMT1 inhibitors are currently under development; yet, we do not fully understand the mechanisms underpinning PRMT1 involvement in tumorigenesis and chemoresistance. Using mass spectrometry-based proteomics, we identified PRMT1 as regulator of arginine methylation in ovarian cancer cells treated with cisplatin. We showed that DNA-dependent protein kinase (DNA-PK) binds to and phosphorylates PRMT1 in response to cisplatin, inducing its chromatin recruitment and redirecting its enzymatic activity toward Arg3 of histone H4 (H4R3). On chromatin, the DNA-PK/PRMT1 axis induces senescence-associated secretory phenotype through H4R3me2a deposition at pro-inflammatory gene promoters. Finally, PRMT1 inhibition reduces the clonogenic growth of cancer cells exposed to low doses of cisplatin, sensitizing them to apoptosis. While unravelling the role of PRMT1 in response to genotoxic agents, our findings indicate the possibility of targeting PRMT1 to overcome chemoresistance in cancer.

INTRODUCTION

Arginine (R)-methylation is a protein post-translational modification (PTM) that occurs both on histones and non-histone proteins, implicated in the physio-pathological regulation of different cellular processes (Bedford and Clarke, 2009; Bedford and Richard, 2005). Three types of R-methylation exist in mammalian cells: mono-methyl-R (MMA), asymmetric di-methyl-R (ADMA), and symmetric di-methyl-R (SDMA). This PTM has attracted increasing interest due to its emerging role in several biological pathways, including RNA splicing and metabolism, translation, DNA damage signaling, and inflammatory response (Blanc and Richard, 2017; Kim et al., 2016). Nonetheless, the comprehensive study of R-methylation has been hindered by several technical challenges, thus delaying the global analysis of this modification compared to others, such as serine threonine/tyrosine (ST/Y)-phosphorylation, lysine (K)-ubiquitination, and acetylation (Wang et al., 2017). The recent optimization of biochemical workflows for the affinity enrichment of R-methylated peptides from total protein extracts, coupled to state-of-the-art liquid chromatography-tandem mass spectrometry (LC-MS/MS), as well as automated pipelines for MS-data analysis, has led to the significant expansion of the annotated human R-methyl proteome (Larsen et al., 2016; Massignani et al., 2019; Musiani et al., 2019; Sylvestersen et al., 2014).

In mammals, R-methylation is catalyzed by a family of nine PRMTs, of which PRMT1 is the predominant, as it mediates the deposition of most arginine methylation in human cells (Tang et al., 2000). On the contrary, no bona fide R-demethylases have been identified so far, leaving unanswered the question whether R-methylation is reversible or not (Guccione and Richard, 2019).

The critical role played by PRMT1-dependent protein methylation is underscored by the fact that PRMT1 loss is embryonic lethal in mice and the derived mouse embryonic fibroblasts display severe genetic defects, such as polyploidy and spontaneous DNA damage (Yu et al., 2009). Interestingly, this specific phenotype suggests that this enzyme, and the modification set, contribute to the maintenance of genome stability (Boisvert et al., 2005).

PRMT1 is a type I R-methyltransferase that catalyzes MMA and ADMA on an ample panel of protein substrates involved in various cellular processes, including double-strand break (DSB) repair (e.g., MRE11) (Boisvert et al., 2005), RNA processing (e.g., hnRNPA1) (Tang et al., 2000), and transcriptional activation (e.g., through histone H4) (Wang et al., 2001). PRMT1 is overexpressed in various tumors (Cheung et al., 2016), and its level positively correlates with poor clinical outcomes of cancer

This is an open access article under the CC BY-NC-ND license (http://creativecommons.org/licenses/by-nc-nd/4.0/).

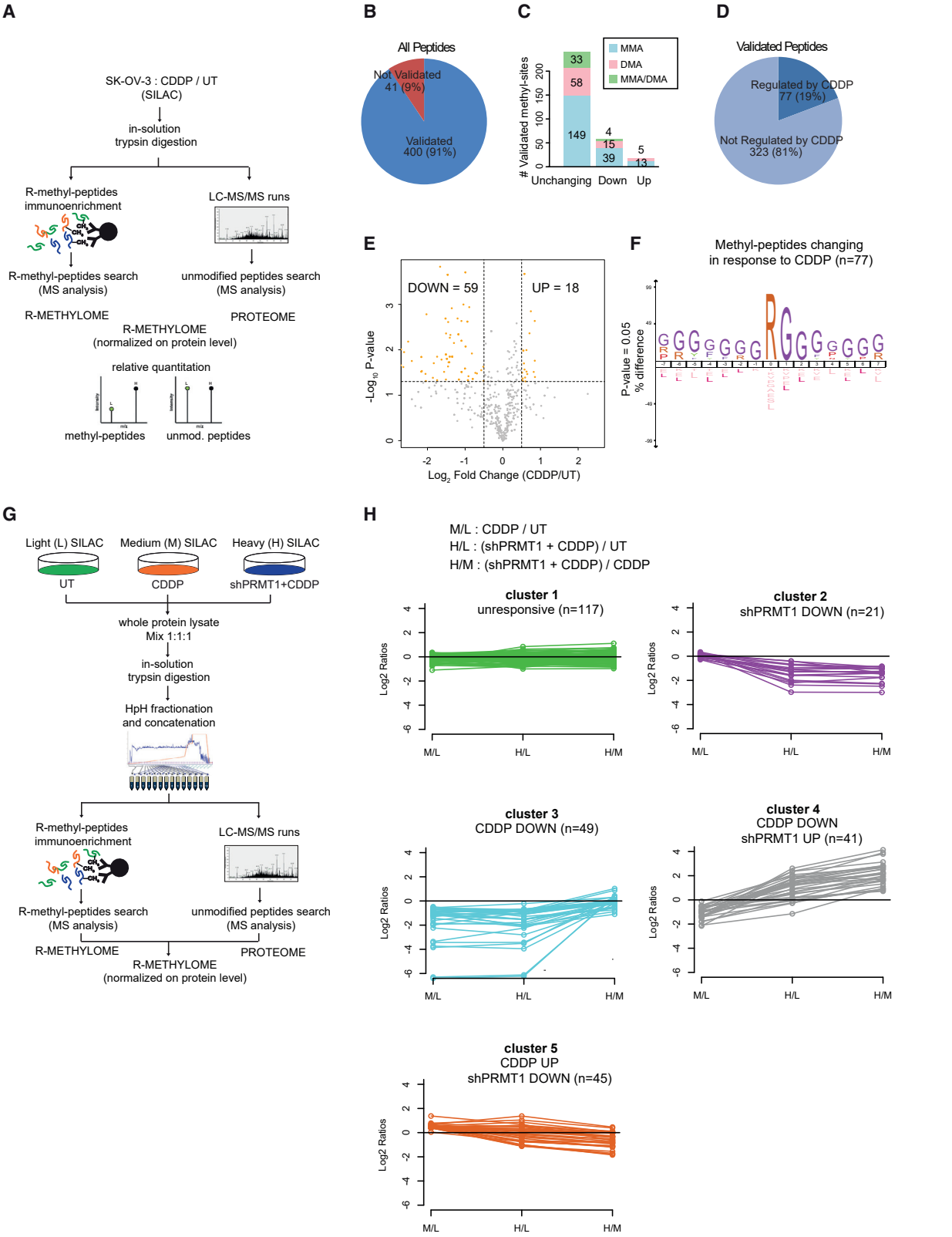

(legend on next page)

patients (Altan et al., 2016). Therefore, PRMT1 is emerging as an attractive target for cancer treatment and several small molecule inhibitors targeting its catalytic activity are under development (Guccione and Richard, 2019).

Despite the increasing interest in the function of PRMTs, our understanding of the impact of R-methylation regulation on most cellular processes is still limited. For instance, the role of PRMT1 in the repair of ionizing radiation-induced DSBs was reported to be due mainly to the modification of a few specific substrates, such as 53BP1 and MRE11, which were found to be methylated by candidate-based approaches (Boisvert et al., 2005). However, a systematic assessment of the effect of PRMT1 on the R-methyl proteome during DNA damage response (DDR) and replication stress response is still missing.

Here, we carried out the MS profiling of protein-R-methylation upon cisplatin (CDDP) in dependence of PRMT1, and observed widespread changes in protein-R-methylation of ovarian cancer cells. In particular, we found decreased methylation on a subset of RNA-binding proteins (RBPs) and increased modification on various chromatin-associated proteins that are linked to the cellular response to genotoxic stress.

We also observed that PRMT1 increases in the chromatin compartment upon replicative stress and that DNA-dependent protein kinase (DNA-PK) is required for this chromatin accumulation. On chromatin, PRMT1 methylates its target H4R3, thus leading to the activation of genes involved in the senescence-associated secretory phenotype (SASP), which protects from apoptosis cells confronted with sustained DNA damage.

Overall, our data show that PRMT1 activity contributes to the adaptive response of cancer cells to replicative stress agents, so that the pharmacological blockade of this regulatory mechanism sensitizes cancer cells to CDDP.

RESULTS

MS-Profiling of PRMT1-Dependent Protein-R-Methylation in Response to CDDP

To study the role of R-methylation in cell response to CDDP, we exploited stable isotope labeling by amino acids in cell culture (SILAC)-based proteomics to analyze global changes of this modification triggered by the drug, in SK-OV-3 ovarian cancer cells. We carried out three independent R-methyl proteomics experiments, each performed in two biological replicates (forward and reverse: see Table S1, and STAR Methods for the experimental details) by combining SILAC labeling with R-methyl-peptides affinity enrichment using anti-*pan* MMA and ADMA antibodies, as well as MS-based analysis (Figure 1A). We thus reproducibly quantified 441 methyl peptides that we orthogonally validated by the heavy methyl SILAC (hmSILAC) strategy (Bremang et al., 2013; Musiani et al., 2019; Ong et al., 2004) to reduce the false discovery rate (FDR) associated to our methyl-peptide dataset. In particular, we compared our dataset with a repository of hmSILAC-labeled methyl sites that was generated using 127 raw files from multiple methyl-proteomics experiments from three distinct human cancer cell lines (Massignani et al., 2019). The majority (400/441) of peptides composing our dynamic methyl proteome were hmSILAC validated and then used for subsequent analysis (Figure 1B). These 400 methyl peptides belonged to 136 proteins and contained 296 methyl sites in total, corresponding to 238 mono-methylation and 115 di-methylation events (Figure 1C; Table S1).

The analysis of the six paired CDDP/untreated (UT) experiments allowed defining statistically significant changes in R-methylation induced by the drug (Figure 1D), with 59 and 18 methyl peptides being significantly down- and upregulated, respectively (Figure 1E). When we carried out a logo analysis on these regulated methyl sites, we found the emergence of the RG/RGG sequence, the well-known PRMT1 consensus motif (Figure 1F; Thandapani et al., 2013). When we linked the CDDP-regulated sites to their respective proteins, we observed that they belonged to 41 proteins, of which 17 were previously described as PRMT1 targets (Table S1; Figure S1A).

Interestingly, we identified among the proteins whose methylation was reduced by the drug mainly RBPs involved in stress granules formation, such as G3BP1, hnRNPA1, and SAM68 (Guil et al., 2006; Henao-Mejia and He, 2009; Matsuki et al., 2013). Instead, among the proteins whose methylation was increased we found various chromatin-associated factors, such as the RNA helicase DDX17 and RBMX, both described to localize to DNA-damaged sites (Adamson et al., 2012), and the chromatin target of PRMT1 (CHTOP), which was shown to recruit PRMT1 to DNA regions containing 5-hydroxymethylcytosine,

Figure 1. Modulation of the Cellular R-Methyl-Proteome in Response to CDDP

(A) Schematic representation of the experimental setup of SILAC labeling coupled with affinity enrichment of methylpeptides, followed by MS analysis with MaxQuant software for methyl-peptide identification and quantification. An aliquot of the input prior to immuno-enrichment was MS analyzed to measure protein levels and used to normalize the values of the respective methylation changes.

(B) Pie chart displaying the percentage of hmSILAC-validated methyl peptides.

(C) Bar graph showing the number of SILAC-quantified and hmSILAC-validated methyl sites grouped based on the modification level and the response to CDDP. DMA, methyl sites exclusively di-methylated; MMA, methyl sites exclusively mono-methylated; MMA/DMA, methyl sites found both mono- and di-methylated.

(D) Pie chart displaying the percentage of the CDDP-regulated and not-regulated methyl peptides that were hmSILAC validated.

(E) Volcano plot showing the methyl peptides significantly changing in response to CDDP treatment. The methyl peptides derived from 6 biological replicates of SILAC-based CDDP/untreated (UT) samples. Significantly regulated peptides have $p < 0.05$ and a CDDP/untreated SILAC ratio > 0.5.

(F) Logo analysis of the dynamically regulated methyl peptides upon CDDP performed with IceLogo, using as background random sequences from the human proteome. The motif is centered on the methylated R.

(G) Scheme of the experimental workflow of triple-SILAC labeling, coupled with RP-HpH fractionation and affinity enrichment of methyl peptides, followed by MS analysis.

(H) Unsupervised clustering analysis of the $\log_2$-transformed SILAC ratios of methyl peptides in response to CDDP and PRMT1 depletion reveals 5 major patterns of changes. Only methyl peptides that were reproducibly identified in the forward and reverse experiments with a SILAC ratio above/below the $\mu \pm 1\sigma$ cutoff were analyzed.

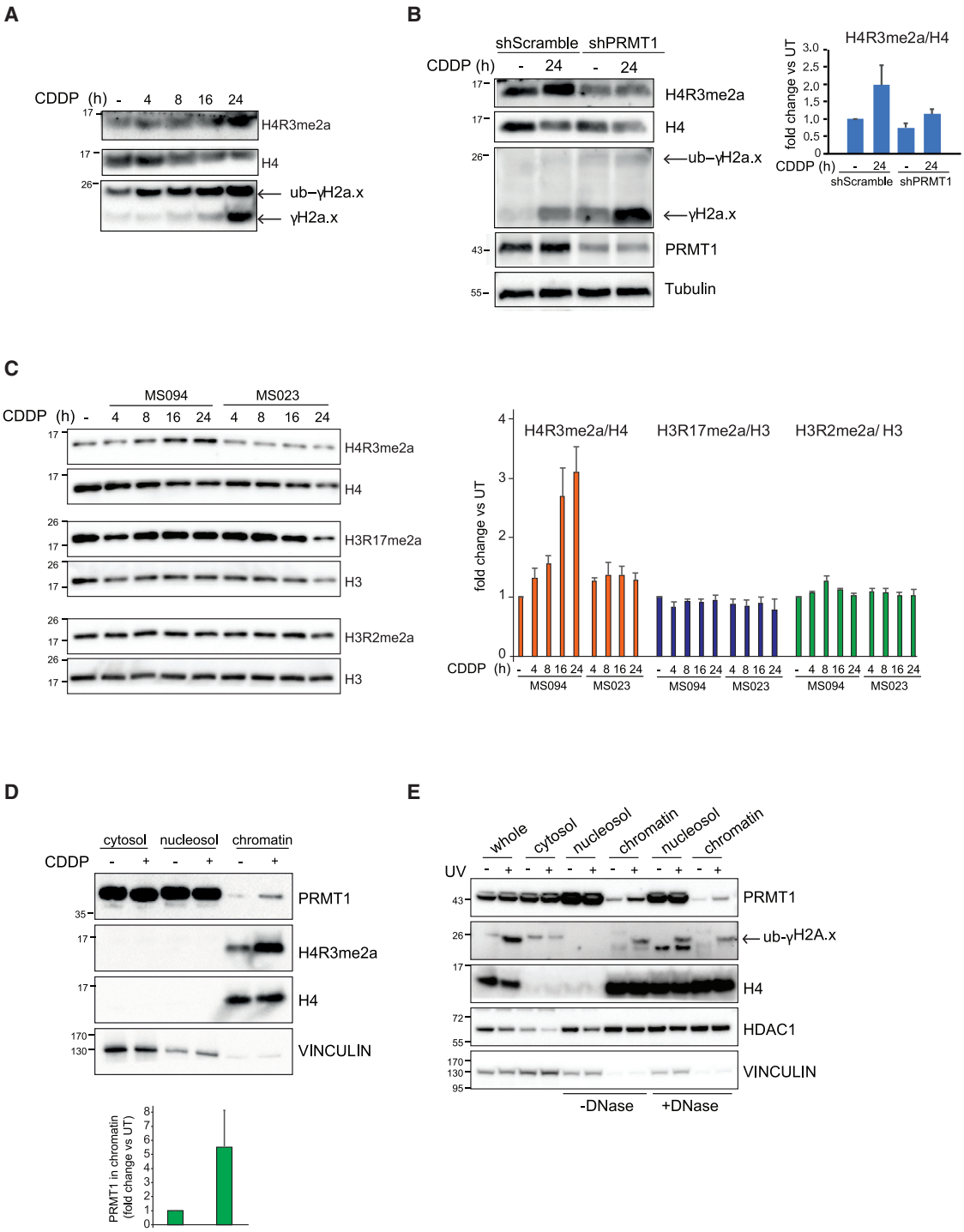

Figure 2. PRMT1 Increases in Chromatin and Triggers H4R3me2a in Response to Replication Stress

(A) Time course WB profiling of H4R3me2a in SK-OV-3 treated with 20 μM CDDP for the indicated time points. The displayed image is representative of 3 biological replicates (n = 3).

(B) Left: WB analysis of H4R3me2a and γH2a.x (both unmodified and mono-ubiquitinated forms) in SK-OV-3 cells infected with lentiviral particles for the expression of either the control short hairpin scramble (shScramble) or a shRNA for PRMT1 and treated with 20 μM CDDP, at the indicated time points. The image displayed is representative of 3 biological replicates (n = 3). Right: quantification of H4R3me2a in cells treated as in (left), normalized over histone H4 and presented as fold change over untreated (UT) shScramble cells. Data displayed represent the mean ± standard deviation (SD) from 3 biological replicates (n = 3).

(legend continued on next page)

leading to H4R3 methylation and transcription activation (Takai et al., 2014).

To better define the role of PRMT1 in the protein R-methylation changes triggered by CDDP, we focused on the triple-SILAC experiment performed from whole cell extracts and assessed the combined effect of CDDP treatment and PRMT1 depletion. For this experiment, we included a step of high-pH reversed-phase liquid chromatography (HpH RPLC) separation prior to the methyl-peptide affinity enrichment, in order to increase the methyl-proteome coverage, as previously described (Batth et al., 2014). We analyzed two biological replicates in "forward" and "reverse" SILAC setups, whereby the medium- and heavy-SILAC labels were swapped among two functional states (Figure 1G). We robustly quantified 334 hmSILAC-validated methyl peptides that belonged to 130 proteins and harbored 234 R sites, corresponding to 188 mono- and 89 di-methylations (Figures S1B and S1C; Table S2).

To address the PRMT1 dependency of the changes induced by CDDP, we compared the regulation of R-methyl peptides elicited by CDDP between control and PRMT1-depleted cells by unsupervised clustering analysis of the peptide SILAC $\log_2$ ratios. Five main clusters emerged, corresponding to distinct patterns of response to CDDP treatment and PRMT1 knockdown and revealing the complexity associated to the R-methyl-proteome dynamics in response to these combined stimuli (Figure 1H; Table S2). Cluster 1 contains methyl peptides unresponsive to CDDP and/or PRMT1 knockdown while cluster 2 contains methyl peptides downregulated by shPRMT1 that we considered as bona fide targets of PRMT1. Cluster 3 includes methyl peptides downregulated by CDDP also upon PRMT1 knockdown whereas cluster 4 comprises methyl peptides whose decrease upon CDDP is reverted upon PRMT1 ablation, likely through substrate scavenging by other PRMTs (Dhar et al., 2013). Cluster 5 contains methyl peptides upregulated by CDDP and reduced in PRMT1-depleted cells, a behavior that indicates them as bona fide PRMT1 targets responding to CDDP. Interestingly, while chromatin-associated proteins were mainly represented in cluster 5, RBPs could be found in all of the other clusters displaying a dynamic behavior (clusters 2–4). We confirmed the MS data by protein immunoprecipitation (IP) followed by western blot (WB) profiling of ADMA on hnRNPA1, which belongs to cluster 4 and whose methylation decreased upon CDDP (Figure S2A) and on PSPC1 that belongs to cluster 5 and whose methylation increased in response to CDDP and was impaired by PRMT1 depletion (Figure S2B). In line, the MMA level of the p82 isoform of DDX17, also belonging to cluster 5, was increased upon CDDP, while this effect was inhibited in PRMT1-depleted cells (Figure S2C).

We observed the following distribution of the different methylation species in clusters 2–5: 85 mono-methylated sites were equally distributed among them, while the 30 di-methylated sites were mainly accumulating in clusters 3 and 5 (Table S2). Of these peptides, more than 70% were asymmetrically di-methylated, as demonstrated by the visual inspection of the respective MS2 spectra, with detection of diagnostic neutral loss ions (Musiani et al., 2019). This evidence corroborates the interpretation that clusters 3 and 5 mainly include PRMT1 targets, in agreement with the dynamic behavior of their methylations.

Overall, our quantitative MS analysis shows that PRMT1 is involved in the protein R-methylation changes observed upon CDDP and raises the question whether this event contributes to the response to genotoxic stress of ovarian cancer cells.

PRMT1 Increases in Chromatin and Triggers H4R3me2a in Response to Replication Stress

The observation that several chromatin-associated proteins are hyper-methylated in a PRMT1-dependent manner in response to CDDP suggests that the activity of this enzyme may be preferentially channeled toward this subcellular compartment. Since the MS analysis did not detect any histone methylated arginines, most likely due to the underrepresentation of histone peptides from tryptic digestions in LC-MS/MS shotgun proteomics (Soldi et al., 2014), we profiled by WB the asymmetric di-methylation of H4R3 (H4R3me2a) in SK-OV-3 cells treated for increasing time intervals with CDDP. We observed a time-dependent increase of this modification (Figure 2A), which was reduced when we knockdown PRMT1 by cell transduction with specific small hairpin RNA (shRNA) carrying lentiviral particles infection, confirming that the change is specifically dependent on this methyl transferase (Figure 2B). As a further confirmation, we observed that the CDDP induction of H4R3me2a was impaired in cells pre-treated with the *pan*-type I PRMT inhibitor MS023 (Eram et al., 2016), and not in those treated with the inactive compound MS094 (Figure 2C). In the same experiment, bulk levels of H3R17me2a and H3R2me2a—set by CARM1 and PRMT6, respectively—did not change significantly upon CDDP, suggesting that these PRMTs are not activated by the drug.

Interestingly, we observed a time-dependent increase of H4R3me2a also in response to other replicative stress inducing agents, such as hydroxyurea (HU), gemcitabine (GEM), and ultraviolet (UV) light, whereas ionizing radiation (IR) increased this methyl mark only marginally and with a different kinetics than the one observed for γH2A.x (Figures S3A–S3C).

(C) Left: time course WB analysis of the indicated histone PTMs in SK-OV-3 treated with 20 μM CDDP following 24 h pre-treatment with either MS094 (10 μM) or MS023 (10 μM). The displayed image is representative of 4 biological replicates (n = 4). Right: quantification of the histone PTMs levels in cells treated as in the left panel, normalized over the total level of the respective histone protein and reported as fold change over untreated (UT) cells. Data displayed represent the mean ± SD from 4 biological replicates (n = 4).

(D) Top: WB analysis of the subcellular fractions of SK-OV-3 cells, untreated or treated with 20 μM CDDP for 24 h. Detection of vinculin and histone H4 shows equal loading of the cytosolic and chromatin fractions, respectively. The displayed image is representative of 4 biological replicates (n = 4). Bottom: quantification of PRMT1 in the chromatin-enriched fraction in the presence or absence of CDDP, normalized over the histone H4 level and expressed as fold change over untreated (UT) cells. Data displayed represent the mean ± SD from 4 independent biological experiments (n = 4).

(E) Chromatin-binding assay of PRMT1 in HeLa cells, irradiated or not with UV 40 J/m^2 for 24 h, with and without DNase treatment of the nuclei before fractionation into nucleosolic and chromatin-enriched compartments. Vinculin and histone H4 detection confirms the equal loading of the cytosol and the chromatin-bound fractions, respectively.

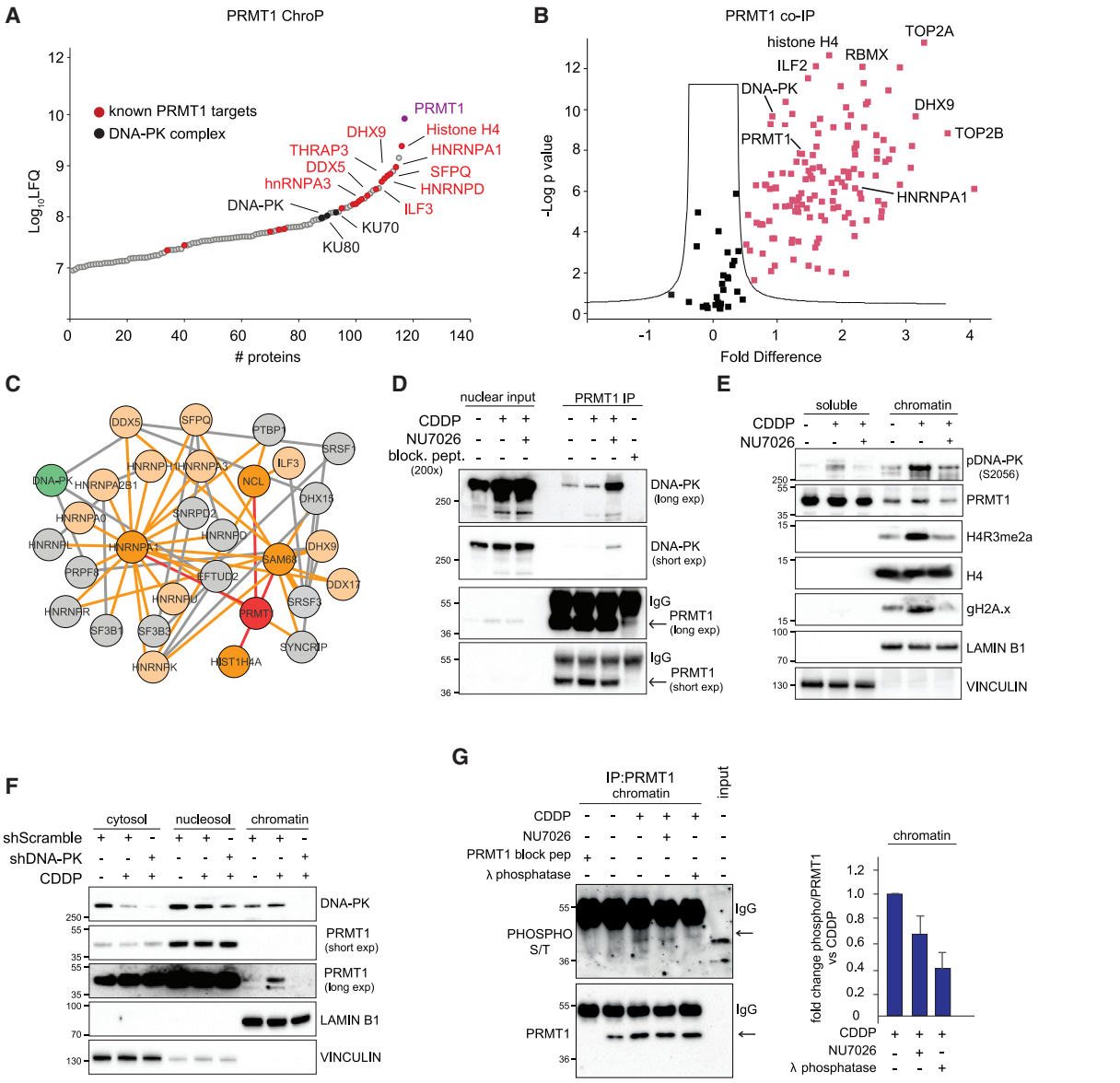

Figure 3. DNA-PK Binds to PRMT1 and Mediates Its Chromatin Recruitment in Response to CDDP

(A) Analysis of PRMT1 interactors within chromatin by ChroP experiment. Intensity-based label free quantification (LFQ) values of proteins unambiguously identified by LC-MS/MS upon PRMT1 immunoprecipitation from SK-OV-3 cross-linked chromatin. Known PRMT1 targets and the DNA-PK holoenzyme subunits are highlighted in red and black, respectively.

(B) Nuclear PRMT1-interaction network analysis by protein co-immunoprecipitation (coIP) followed by LC-MS/MS. Volcano plot displays the proteins significantly enriched in the PRMT1 coIP experiment (red squares) relative to the mock IP, by plotting −log p value over fold difference from three biological replicate experiments. FDR < 0.01, minimal fold change (S0) = 0.4 (n = 3).

(C) Functional analysis of the PRMT1 interactome. Proteins enriched in both the native and cross-linked PRMT1 IPs (coIP and ChroP, respectively) were analyzed using the STRING interaction database and the proteins belonging to the same STRING network were visualized using Cytoscape. Primary and secondary interactors of PRMT1 are displayed in dark and light orange, respectively; PRMT1 and DNA-PK are indicated in red and green, respectively.

(D) CoIP followed by WB analysis from SK-OV-3 cells treated with 20 μM CDDP and 10 μM NU7026; coIPs were carried out in the presence and absence of 200× molar excess of PRMT1 blocking peptide, as indicated. The image displayed is representative of 3 biological replicates (n = 3).

(E) WB analysis of PRMT1 levels in the soluble and chromatin-enriched fractions of SK-OV-3 cells treated for 24 h with CDDP 20 μM, with or without pre-treatment with NU7026 (10 μM). H4R3me2a and γH2a.x were used as markers of PRMT1 activity and activated DDR, respectively. The image displayed is representative of 3 biological replicates (n = 3).

(F) WB analysis of PRMT1 and DNA-PK levels in different subcellular compartments of control (shScramble) and DNA-PK knockdown (shDNA-PK) SK-OV-3 cells, treated or not with CDDP 20 μM for 24 h. The image is representative of 2 biological replicates (n = 2).

(legend continued on next page)

Importantly, less than 7% of cells were Annexin V-positive at 24 h, the latest time point of treatment, confirming that H4R3me2a increase is not a mere consequence of apoptosis (Figure S3D).

Since PRMT1 is constitutively active and localized in both nucleus and cytoplasm at basal state and that its modulation can be achieved by regulating its sub-cellular compartmentalization (Goulet et al., 2007; Herrmann et al., 2005), we reasoned that the protein-R-methylation changes observed upon CDDP could be due to a differential subcellular localization of PRMT1. We thus profiled its level by WB, upon the biochemical separation of SK-OV-3 cells into cytosolic, nucleosolic, and chromatin-enriched fractions. We observed that PRMT1 increased in the chromatin fraction of cells treated with both CDDP and UV irradiation (Figures 2D and 2E), while the subcellular distribution of another chromatin modifier used as control, i.e., HDAC1, did not follow the same trend (Figure 2E). The DNase treatment of nuclei prior to fractionation released PRMT1 from chromatin (Figure 2E, compare lane 8 to lane 12), confirming the specific increase of PRMT1 in the chromatin compartment under replicative stress.

Together, these data demonstrate that replicative stress-inducing agents lead to increased association of PRMT1 to chromatin, where the enzyme directs its catalytic activity toward histone H4.

DNA-PK Binds to PRMT1 and Mediates Its Chromatin Recruitment in Response to CDDP

PRMT1 does not possess a recognizable DNA-binding domain; hence, we reasoned that its chromatin accumulation during replication stress could be mediated by the interaction with other DNA-binding proteins. We thus carried out a MS-based analysis of the PRMT1-interaction network in the chromatin context, applying the chromatin proteomics (ChroP) approach, which couples preparative chromatin immunoprecipitation (ChIP) to MS-based proteomics (Soldi and Bonaldi, 2013, 2014). We identified known PRMT1 binders in the PRMT1 ChroP, such as histone H4 and the non-histone proteins hnRNPA1 and ILF3 (Figure 3A; Table S3). We further investigated the nuclear PRMT1 interactome in native conditions, by MS analysis of PRMT1 co-immunoprecipitation (coIP), using the SK-OV-3 nuclear extract as input. From the label-free quantification of proteins in 3 coIP replicates, we identified 129 proteins significantly co-enriched with PRMT1, whose specificity was verified by repeating the coIP in the presence of a large excess of a soluble peptide competing with the bait for the binding to the antibody, followed by the assessment of the selective eviction of the bait and the relative interactors (Figure 3B; Table S3). By intersecting these two interactomic datasets, we identified 49 proteins that appear specifically co-enriched with PRMT1 and represent the nuclear PRMT1 interaction network (Figure 3C; Table S3). This is characterized by the overrepresentation of various RBPs previously known as direct PRMT1 targets, such as Sam68 (Côté et al., 2003) and hnRNPA1 (Wada et al., 2002), and whose methylation was indeed found to be dynamically regulated in the triple-SILAC methyl-proteomics experiment (Table S3); these results are in line with previous evidence of the preferential affinity of PRMT1 toward its own enzymatic substrates (Rust et al., 2014).

Interestingly, among the identified interactors we found DNA-PK, the catalytic subunit of the non-homologous end joining (NHEJ) DNA-PK complex, which is encoded by the *PRKDC* gene. WB probing of PRMT1 co-IP proteins confirmed that PRMT1 and DNA-PK interact in SK-OV-3 cells irrespective of CDDP treatment and that the interaction between the two proteins is increased when the cells are pre-treated with the specific DNA-PK inhibitor NU7026 (Willmore et al., 2004; Figure 3D). Interestingly, the increased interaction of PRMT1 with DNA-PK upon NU7026 treatment is reminiscent of the behavior of kinase dead mutants, which trap their substrates in the binding pocket leading to an increased binding; in this case, our results suggest that the ATP-competitive inhibitor NU7026 may affect the DNA-PK/PRMT1 interaction in a similar manner (Deminoff et al., 2006; Iliuk et al., 2012). The specificity of the DNA-PK/PRMT1 interaction was also corroborated by performing the PRMT1 coIP in the presence of an excess of the competing peptide, leading to selective reduction of DNA-PK (Figure 3D).

We then tested whether PRMT1 recruitment to chromatin could be dependent on DNA-PK activity by treating SK-OV-3 cells with NU7026 prior to CDDP, fractionating cells into soluble and chromatin compartments, and profiling PRMT1 by WB. We found that NU7026 reduced both PRMT1 recruitment and H4R3me2a accumulation on chromatin (Figure 3E). The efficiency of the drug was assessed by confirming that the phosphorylation of DNA-PK induced by CDDP was blocked. Last, the functional link between DNA-PK activity and PRMT1 recruitment to chromatin was further supported by the results obtained following DNA-PK depletion by RNA interference (RNAi) (Figure 3F).

In light of these data and of published evidence of PRMT1 phosphorylation at seven potential serine/threonine (S/T) sites (Hornbeck et al., 2015), we tested whether DNA-PK can phosphorylate PRMT1. We measured PRMT1 phosphorylation by WB with a *pan*-phospho-S/T antibody upon protein enrichment by IP, using as input the chromatin fraction from cells treated with CDDP, which were either pre-treated or not with NU7026. The phosphorylation of chromatin-bound PRMT1 in CDDP-treated cells was reduced when the pre-treatment with NU7026 was performed (Figure 3G, arrow). Notably, treatment of the chromatin fraction from CDDP-stimulated cells with λ phosphatase led to a further decrease of the phosphorylation signal of the IPed PRMT1, which confirmed that the signal detected with the *pan*-phospho-S/T antibody is a true phosphorylation (Figure 3G). We confirmed that DNA-PK phosphorylates PRMT1 by repeating the experiment in DNA-PK RNAi-depleted cells and observing a reduced PRMT1 phosphorylation upon CDDP exposure, similarly to NU7026 treatment (Figure S3E).

(G) Left: WB analysis of PRMT1 phosphorylation, following protein IP and using as input the chromatin fraction of SK-OV-3 cells, treated with 10 μM NU7026 and 20 μM CDDP for 24 h, as indicated. PRMT1 phosphorylation was detected using a *pan*-phospho-S/T antibody. The arrows indicate the band corresponding to phosphorylated and total PRMT1, detected by the *pan*-phospho S/T (top) and PRMT1 (bottom) antibodies, respectively. The image is representative of 2 biological replicates (n = 2). Right: quantification of the phosphorylated form of PRMT1 normalized over the total level of PRMT1 in the chromatin extract and expressed as fold change over CDDP treated cells. Data displayed represent the mean ± variation from 2 biological replicates (n = 2).

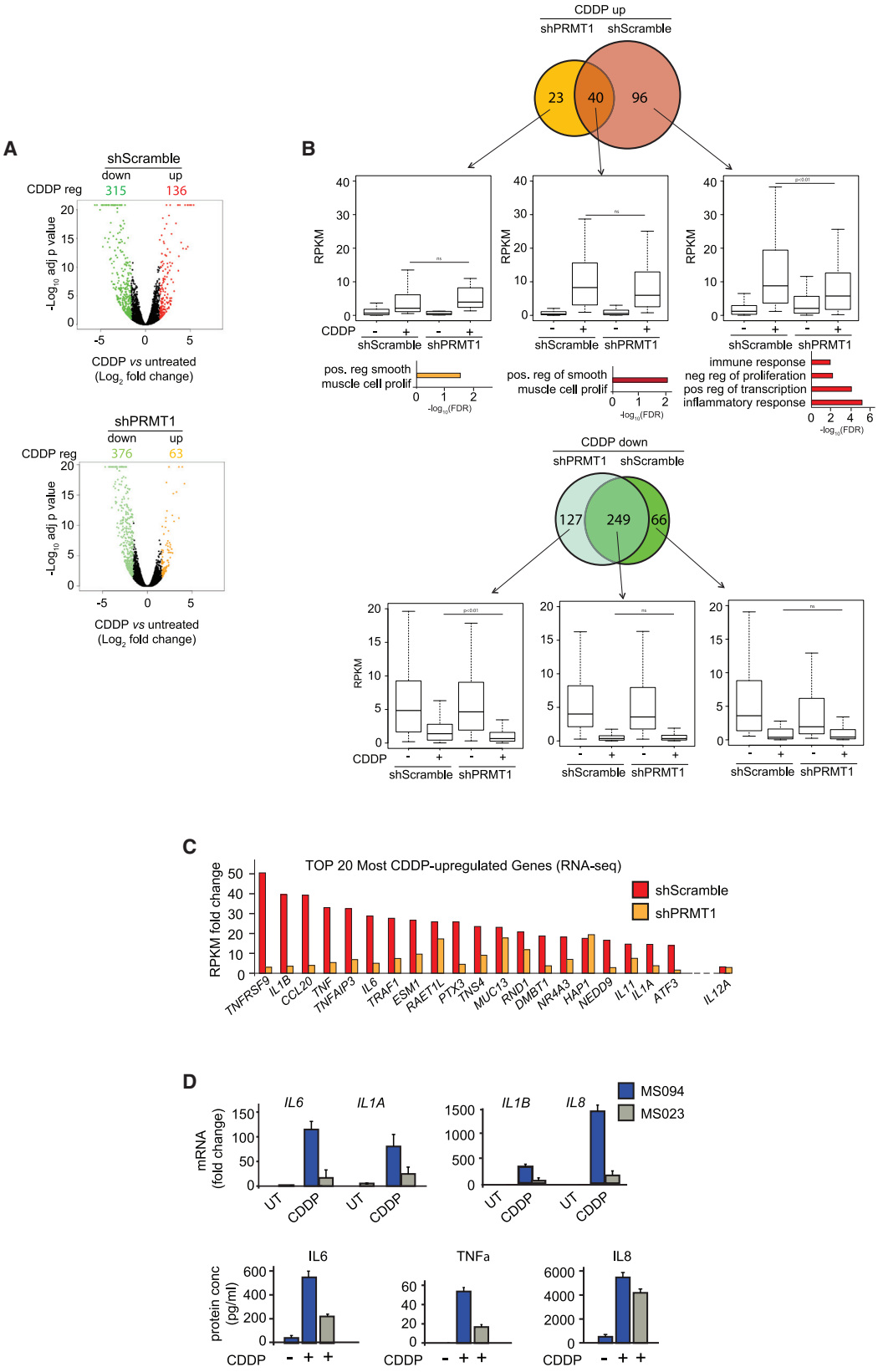

(legend on next page)

These data indicate that DNA-PK interacts with PRMT1 and that its kinase activity is required for CDDP-triggered recruitment of PRMT1 to chromatin. Furthermore, the observation that in CDDP-treated cells the chromatin-bound PRMT1 is phosphorylated and that the phosphorylation signal is diminished upon NU7026 suggests that this modification may be the signal directing PRMT1 to chromatin. Whether DNA-PK phosphorylates PRMT1, directly or indirectly, remains to be assessed.

PRMT1 Mediates the Activation of the SASP during Replicative Stress Response

As a histone modifier deposing asymmetric di-methylation on H4R3, PRMT1 acts as a transcriptional coactivator (Wang et al., 2001). Recently, H4R3me2a has been also associated to the transcriptional-mediated maintenance of stem cell-like properties of esophageal squamous cell carcinoma (Zhao et al., 2019).

Prompted by the observation of the PRMT1-dependent increase of H4R3me2a upon treatment with different replication stress agents, we set up to investigate the transcriptional response of SK-OV-3 upon CDDP, in dependence of PRMT1 by RNA sequencing (RNA-seq) analysis (Figures 4A and S4A): while at basal conditions no major changes were observed following PRMT1 ablation (Figure S4B), significant differences in mRNA levels were measured upon CDDP treatment between control and PRMT1-silenced cells (Figure 4A; Table S4). In line with the transcriptional repression typically associated to the DNA damage response (Gentile et al., 2003), we found that CDDP caused the downregulation of 315 genes and the upregulation of 136 genes (Figure 4A, top panel).

When focusing on the dependency of the CDDP-triggered transcriptional response on PRMT1, we observed that the ~1:2.3 ratio between the upregulated and the downregulated genes in control cells shifted to ~1:6 in PRMT1-depleted cells, due to the further reduction in the number of the upregulated genes (63) (Figure 4A, bottom panel). Moreover, by intersecting the CDDP-differentially regulated genes in the presence or absence of PRMT1, we observed that 96 out of the 136 upregulated genes in control cells were not induced when PRMT1 was depleted, indicating that their upregulation by CDDP is truly dependent on PRMT1 (Figure 4B, top panel). Through functional analysis of the genes induced by CDDP in a PRMT1-dependent fashion, we found that the Gene Ontology (GO) terms ''inflammatory response'' and ''immune response'' were specifically enriched, while the genes induced by CDDP independently from PRMT1 were slightly enriched in the generic functional category ''positive regulation of smooth muscle cell proliferation.'' On the contrary, no GO categories emerged as enriched in the genes downregulated by CDDP, irrespective of PRMT1 presence/absence (Figure 4B, bottom panel). Interestingly, within the 20 top-induced genes in control cells, the inflammatory genes belonging to the SASP response (Salama et al., 2014), such as *IL1A*, *IL1B*, *IL6*, and *TNF*α, were overrepresented (Figure 4C). The expression of IL12α, considered a non-SASP-associated cytokine (Davalos et al., 2010), did not display PRMT1 dependency, which confirmed that PRMT1 sustains specifically the SASP-transcriptional program (Figure 4C).

SASP consists in the expression of various growth factors and inflammatory-like cytokines triggered in response to various stress conditions. In cells experiencing a persistent replicative stress, SASP enforces the maintenance of cell-cycle arrest, thus providing time for lesion repair (Coppé et al., 2010). We first validated the RNA-seq data by quantitative real-time PCR profiling of a panel of representative SASP genes in both SK-OV-3 (Figure S4C) and HeLa cells (Figure S4D). Then, we evaluated the role of PRMT1 in SASP onset, following GEM, employed as part of the second-line treatment in platinum-resistant advanced ovarian cancer patients (Bruzzone et al., 2011). GEM triggered *IL1A*, *IL1B*, and *IL6* transcription, which was however abrogated in PRMT1-knockdown cells (Figure S4E). Thus, we could conclude that PRMT1 plays a role in the modulation of SASP in non-inflammatory cells undergoing replicative stress response.

We also observed that MS023 abrogated the CDDP-induced SASP genes expression (Figure 4D, top panel) and, on the same line, that a multiplexed bead-based immunoassay analysis showed a significant reduction of all the tested cytokines in the conditioned medium of MS023 pre-treated cells, compared to that of cells treated with MS094 (Figure 4D, bottom panel). We also evaluated the involvement of DNA-PK in the regulation of SASP: the NU7026 inhibitor blocked SASP gene induction in response to CDDP (Figure S4F), which indicates that the SASP transcriptional program is mediated by the DNA-PK-PRMT1 regulatory axis.

To test whether PRMT1-mediated SASP gene induction involves H4R3me2a, we profiled this mark by ChIP-qPCR at the promoters of a set of canonical SASP genes, at basal state and upon CDDP. We observed a mild increase of H4R3me2a upon CDDP at the promoters of four SASP genes analyzed, which did not occur on a negative control genomic region (Figure S4G); in line with the gene expression results, we observed that NU7026 pre-treatment partially reduces H4R3me2a binding in three out of the four genes analyzed.

Figure 4. PRMT1 Mediates the Activation of the SASP during Replicative Stress Response

(A) Volcano plots of RNA-seq analysis of shScramble (top) and shPRMT1 SK-OV-3 cells (bottom), harvested 24 h after treatment with 20 μM CDDP. Numbers of genes significantly upregulated (red and orange) and downregulated (dark and light green) are shown (4-fold change cutoff, adjusted [adj] $p \leq 0.05$).

(B) Overlap of genes significantly up- (top) or down- (bottom) regulated by CDDP whereby control and PRMT1 knockdown cells are compared. Gene Ontology (GO) analysis of the CDDP upregulated genes in shScramble (red) and shPRMT1 (orange) cells. No specific GO categories were significantly enriched in the CDDP-downregulated genes between control (dark green) and PRMT1 knockdown (light green) cells.

(C) RNA-seq data of the 20 most upregulated genes by CDDP, in control (red) and PRMT1-depleted (orange) cells, displayed as RPKM values.

(D) Validation of RNA-seq by quantitative real-time PCR and WB profiling of mRNA (top) and protein (bottom) levels of the indicated genes, from SK-OV-3 cells pre-treated for 24 h with either MS023 or MS094 before subsequent incubation with 20 μM CDDP for 24 h. Data represent the mean ± variation from 2 biological replicates (n = 2) (top) and 4 technical replicates (bottom), respectively.

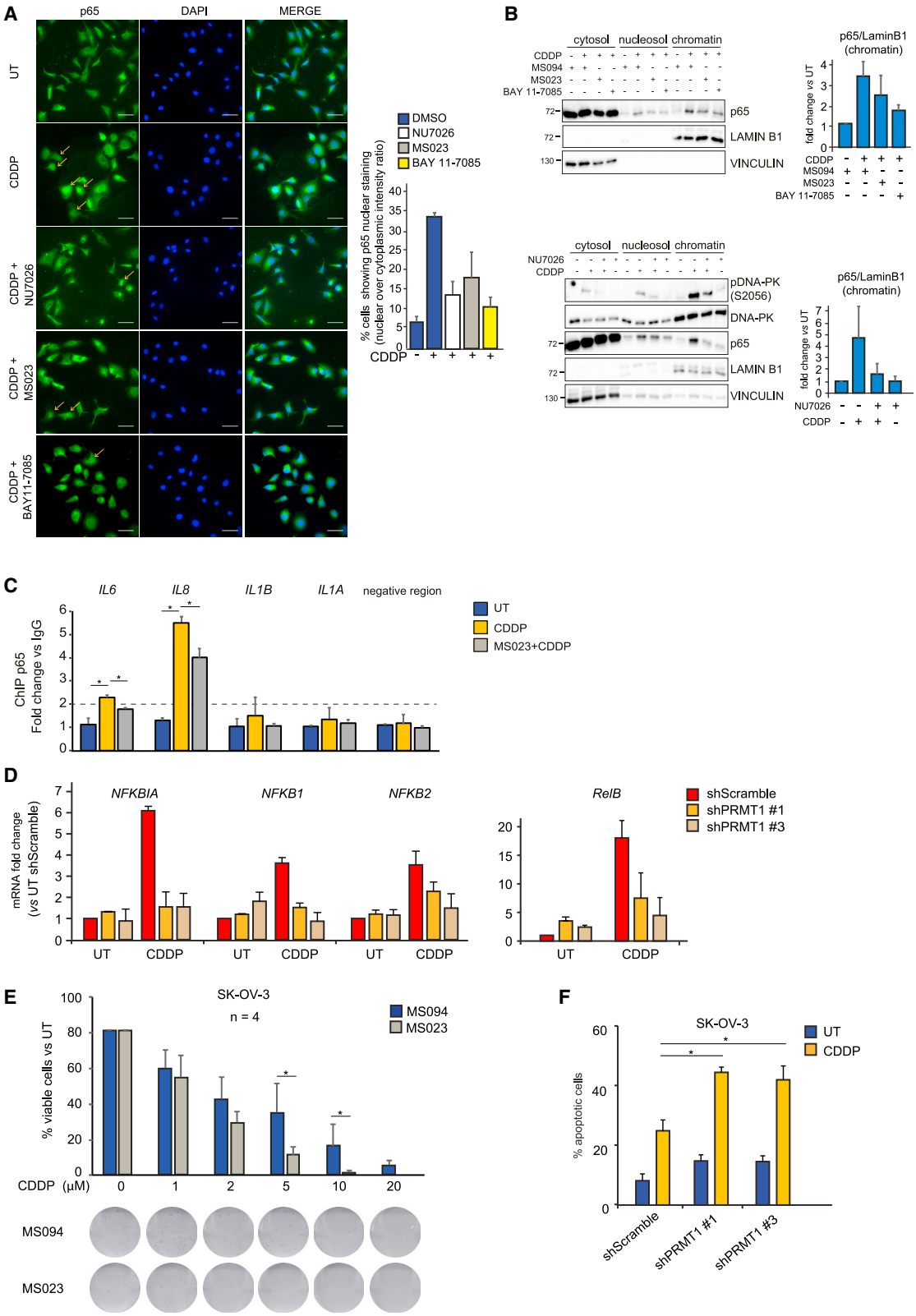

(legend on next page)

PRMT1 Inhibition Dampens the Activation of the NF-κB Pathway and Sensitizes Cells to CDDP

Nuclear factor κB (NF-κB) is the master regulator of SASP (Salminen et al., 2012) and its activation in the context of DDR occurs downstream of a complex signaling network that originates from the detection of the DNA lesions and is mediated by the activity of the three major PIKKs (ATM/ATR/DNA-PK) and of the p38 MAPK (Freund et al., 2011; Sabatel et al., 2011). Since PRMT1 has been reported to regulate the NF-κB-dependent gene expression (Hassa et al., 2008; Reintjes et al., 2016) and given our experimental evidence showing that SASP genes are regulated by PRMT1, we set to investigate whether PRMT1 induces SASP through the modulation of the NF-κB pathway. We first profiled the effect of CDDP on the subcellular localization of p65, the main subunit of the NF-κB transcription factor family, whose cytosol-to-nucleus translocation is associated to NF-κB activation (Maguire et al., 2011): both immunofluorescence (IF) and WB analysis following subcellular fractionation showed that p65 nuclear translocation is induced by CDDP and this effect is reduced when cells are pre-treated with the NF-κB inhibitor BAY-117085, as expected, and NU7026 (Figures 5A and 5B, bottom panel). In addition, we observed a mild but reproducible reduction of p65 nuclear translocation also when we pre-treated cells with MS023 (Figures 5A and 5B, top panel).

Reflecting on the evidence that the SASP transcriptional program is impaired upon PRMT1 depletion and/or pharmacologically inhibition, we asked whether PRMT1 catalytic activity may facilitate p65 binding to the SASP promoter genes by H4R3me2a deposition at the same regulatory regions. By ChIP-qPCR analysis, we found that, upon CDDP, p65 binds to the promoters of two out of four investigated SASP genes, namely *IL6* and *IL8*, with a trend similar to H4R3me2a, while not binding to an unrelated genomic region, used as negative control (Figure 5C). Moreover, p65 binding to these two promoters was reduced by MS023/CDDP co-treatment in a statistically significant manner (Figure 5C). These data suggest that di-methylation of H4R3 by PRMT1 at the promoter of SASP genes correlates with the p65 binding at the same genomic regions, thus pointing towards a possible role of H4R3me2a in sustaining the activation of the NF-κB-SASP axis upon CDDP.

To further verify the role of PRMT1 on p65 activation, we measured the transcription of the NFKBIA gene, which encodes IκBα (the major NF-κB inhibitor protein), and of NFKB1, NFKB2, and RELB (Huxford and Ghosh, 2009), which are direct p65-transcriptional targets. As expected, we observed that their induction following CDDP was impaired upon PRMT1 knockdown (Figure 5D). On the same line, both MS023 and BAY-117085 impaired the CDDP-induced transcription of NFKBIA, as well as of other SASP genes tested (Figure S4H).

SASP is considered a mechanism underpinning resistance to chemotherapy, achieved through the protection of tumor cells from drug-induced apoptosis through the maintenance of the cell-cycle arrest upon DNA lesions detection (Salminen et al., 2011; Sun et al., 2018). Our findings suggest that PRMT1 may have a role in the protection of cancer cells from the deleterious effects of replicative stress agents. To assess this hypothesis, we measured the clonogenic survival of SK-OV-3 cells exposed to increasing doses of CDDP in the presence of either MS023 or MS094 and the results showed that PRMT1 inhibition sensitizes cells to the drug (Figure 5E). Furthermore, PRMT1 depletion sensitized SK-OV-3 cells to CDDP-triggered apoptosis, as measured by increased Annexin V binding and DAPI staining (Figure 5F).

Altogether our study reveals a role for PRMT1 in mediating the transcriptional SASP program in cancer cells subjected to sustained replicative stress and supports the concept of the use of PRMT inhibitors in combination with conventional

Figure 5. PRMT1 Inhibition Dampens the Activation of the NF-κB Pathway and Sensitizes Cells to CDDP

(A) Left: representative IF image analysis of p65 localization in SK-OV-3 cells, untreated and treated with 20 μM CDDP, alone or in combination with 20 μM NU7026, 10 μM MS023, and 1 μM BAY11-7085 for 24 h. Immunostaining of p65 and DAPI staining (for nuclei visualization) and the respective merged IF images are displayed. Images were taken using a 40× dry objective, and a scale bar of 50 μM has been included in each figure. The images displayed are representative of 3 biological replicates (n = 3). Right: percentage of cells positive for p65 nuclear staining based on the ratio of the nuclear versus cytoplasmic p65 fluorescence mean intensity values (ratio ≥ 1.1) and expressed over the total number of cells (DAPI positive, n > 200 cells for each condition). The images were automatically quantified from 3 biological replicates (n = 3) using an *in-house* developed plug-in of ImageJ and data represent the mean ± SD of the 3 biological replicates (n = 3).

(B) Left: WB analysis of p65 cellular localization after sub-cellular fractionation of SK-OV-3 cells, treated or not with 20 μM CDDP for 24 h, alone or in combination with 10 μM MS023 and 1 μM BAY 11-7085 (top panel), and 10 μM NU7026 (bottom panel). Detection of vinculin and lamin B1 confirms equal loading of the soluble and insoluble fractions, respectively. pDNA-PK levels show the activation of DNA-PK in response to CDDP treatment and the impairment of its activity in cells pre-treated with NU7026. The image displayed is representative of 3 biological replicates (n = 3). Right: quantification of p65 protein amount in the chromatin fraction of cells treated as in the left panel. Data were normalized over lamin B1 signal and displayed as fold change over the untreated (UT) cells. Data represent mean ± SD from 3 biological replicates.

(C) ChIP-qPCR of p65 and immunoglobulin G (IgG), used as negative control, from SK-OV-3 cells treated or not with 20 μM CDDP for 24 h in the presence or absence of 10 μM MS023. Data were normalized over the respective input and are displayed as fold enrichment over the respective IgG control. Data represent the mean ± variation from 2 biological replicates (n = 2). The dashed line is set to 2, which indicates the 2-fold chromatin immuno-enrichment over the respective IgG control. Statistical significances were determined by applying the unpaired two-tailed t test. *p < 0.05; **p < 0.01

(D) Quantitative real-time PCR analysis for profiling the mRNA of the indicated genes belonging to the NF-κB family in SK-OV-3 cells treated with CDDP (20 μM for 24 h) upon PRMT1 knockdown with the indicated shRNA constructs. Data represent mean ± variation from 2 biological replicates (n = 2).

(E) Clonogenic survival assay of SK-OV-3 cells pre-treated with MS094 or MS023 in response to the indicated doses of CDDP. Cells were pre-treated for 24 h with either MS094 or MS023 and then treated for 2 h with CDDP before drug washout. Cells were grown for 6 days and then stained with Crystal violet and quantified using ImageJ. Data represent mean ± SD from 4 biological replicates (n = 4). Statistical significances were determined applying the unpaired 2-tailed t test. *p < 0.05.

(F) Apoptosis assay after 72 h of CDDP (20 μM) exposure of control and PRMT1 knockdown SK-OV-3 cells (shPRMT1#1, #3) analyzed by flow cytometry. Data represent mean ± SD from 3 biological replicates (n = 3). Statistical significances were determined using ANOVA two-factor test; *p < 0.05.

chemotherapeutic agents to sensitize cancer cells and reduce chemotherapy resistance and eventually tumor relapse.

DISCUSSION

In this study, we unravel the role of PRMT1, and its mediated protein R-methylation, in the response of cancer cells to the replicative stress triggered by genotoxic drugs.

The methyl-proteomics analysis in response to CDDP revealed some changes in protein-methylation that can be specifically ascribed to PRMT1 activity; however, we cannot exclude that other PRMTs may also be involved

Interestingly, we observed a more prominent downregulation of methylation in various RBPs. Since R-methylation is known to modulate various RBPs by either affecting their nuclear/cytoplasmic localization or their protein-RNA and protein-protein interactions, as well as liquid-liquid phase separation (Kedersha et al., 2013; Thomas et al., 2011), the observed hypo-methylation of this set of proteins may be mechanistically linked to the formation of stress granules (SGs), known to be triggered by genotoxic agents. This interesting hypothesis is supported by the evidence that arginine demethylation of G3BP1 promotes SGs assembly (Tsai et al., 2016); however, further investigations will allow us to assess systematically, beyond individual cases, if and how PRMT1-dependent protein R-methylation can modulate SGs formation.

With an opposite trend to RBPs, various chromatin factors—such as DDX17, RBMX, and CHTOP—displayed increased methylation upon CDDP, which indicates that the activity of PRMT1 is directed toward the chromatin compartment during replicative stress response. As a perspective, it will be interesting to investigate whether R-methylation of other chromatin-bound PRMT1 substrates beyond H4R3 are involved in the nuclear response of tumor cells to genotoxic drugs, as already reported for MRE11 and 53BP1 (Boisvert et al., 2005; Yu et al., 2012).

Our experimental evidence indicates that DNA-PK, which is activated in response to genotoxic stress, is upstream of PRMT1 recruitment to chromatin and consequent H4R3me2a deposition. We hypothesize that PRMT1 phosphorylation triggered by this kinase may modulate its activity, either in specific cellular compartments, or on a selected set of substrates. Different scenarios supporting this model remain to be assessed: one possibility is that DNA-PK modulates the substrate affinity of PRMT1 through phosphorylation, in line with a previous study demonstrating that PRMT1 phosphorylation at tyrosine 291 can regulate the differential affinity of the enzyme toward its own substrates (Rust et al., 2014). Alternatively, PRMT1 phosphorylation could directly favor PRMT1 accumulation on chromatin, as it was recently shown for PRMT1 phosphorylation mediated by CSNK1a1 (Bao et al., 2017).

RNA-seq analysis allowed dissecting the impact of the DNA-PK/PRMT1/H4R3me2a signaling cascade on transcription, revealing that PRMT1 mediates the activation of SASP genes. Although the increased deposition of H4R3me2a at the CDDP-induced pro-inflammatory genes fits with the well-documented association of this methyl mark to actively transcribed regions (Zhao et al., 2019), we could not acquire H4R3me2a ChIP-seq data with the only antibody available (Active Motif), thus preventing the genome-wide assessment of the CDDP-induced changes of this methyl mark. Hence, the poor performance of this antibody in the ChIP setup is to be taken into account. The availability of better-performing ChIP-seq grade antibodies against this methyl_mark will be greatly beneficial in addressing the role of PRMT1 in transcriptional regulation during cisplatin response. Also, we cannot exclude that the activity of other PRMTs may be involved in the regulation of SASP: first, because MS023 is a type I inhibitor (Eram et al., 2016) not uniquely selective for PRMT1 and, second, because the observed downregulation of several methyl sites in response to cisplatin may lead to the substrate scavenging effect by other PRMTs, including the type II enzymes, as strongly suggested by the dynamic behavior of methyl peptides in cluster 4 (Figure 1H).

Nevertheless, the evidence that PRMT1-depleted cells were not able to induce the expression of SASP genes supports the concept that PRMT1 is specifically involved in this transcriptional response to genotoxic stress. In particular, PRMT1 methylation of R3 of histone H4 at promoters of the SASP upon CDDP treatment seems to correlate with p65 binding, suggesting that this histone mark may participate in chromatin changes that facilitate or stabilize p65 to the promoters of these genes.

The harmful effects of chemotherapy drugs in cancer cells reside in the capability to induce apoptosis when DNA lesions are not efficiently repaired. In this scenario, SASP-mediated cell-cycle arrest represents a barrier that preserves cells from death commitment, hence leading to drug resistance. Importantly, SASP is also triggered *in vivo* in response to CDDP and other DNA-damaging chemotherapeutics (Coppé et al., 2008), thus limiting the effectiveness of anticancer therapies that are based on genotoxic stress. We demonstrate here that PRMT1 mediates the onset of SASP and protects cells from the cytotoxic effect of CDDP, including drug-induced apoptosis. Hence, targeting of PRMT1 by small molecule inhibitors may provide a route to overcome SASP and to increase the effectiveness of CDDP-based chemotherapy on tumors.

STAR★METHODS

Detailed methods are provided in the online version of this paper and include the following:

- KEY RESOURCES TABLE
- LEAD CONTACT AND MATERIALS AVAILABILITY
- EXPERIMENTAL MODEL AND SUBJECT DETAILS
  - Cell culture conditions and reagents
- METHOD DETAILS
  - SILAC and heavy methyl SILAC cell culture conditions
  - Vectors and infections
  - Cell lysis, sub-cellular fractionation and Western Blot analysis
  - PRMT1 protein co-Immunoprecipitation (PRMT1 co-IP)
  - PRMT1 cross-linked chromatin immunoprecipitation (PRMT1 X-ChroP)
  - In-gel digestion of immunoprecipitated proteins

SUPPLEMENTAL INFORMATION

Supplemental Information can be found online at https://doi.org/10.1016/j.celrep.2019.12.061.

ACKNOWLEDGMENTS

We thank F. d'Adda di Fagagna and V. Costanzo for critical reading of the manuscript, the Structural Genomic Consortium (SGC, Toronto, Canada) for providing the MS023 and MS094 compounds, C. Toscani for support with the ChIP-qPCR experiment, C. Soriani and S. Rodighiero of the IEO Imaging Unit for generating the ImageJ plug-in for the automatic analysis of IF images, Fabio Bedin for the assistance with the analysis of the RNA-seq data, and all members of the T. Bonaldi laboratory for helpful discussions. Research activity in the T.B. laboratory has been supported by grants from the Italian Association for Cancer Research (IG-2018-21834) and the CNR-EPIGEN flagship project and the Italian Ministry of Health (Bando Giovani Ricercatori, Conv. n. 061/GR-2009-1580495). D. Musiani was supported by a Fondazione Umberto Veronesi (FUV) fellowship and a Fondazione Istituto Europeo Oncologico (FIEO) fellowship. R.G. was supported by the Fondazione CRUI–PhD ITalents programme (144770571). This work was also partially supported by the Italian Ministry of Health with Ricerca Corrente and 5x1000 funds.

AUTHOR CONTRIBUTIONS

D. Musiani and R.G. designed and performed the experiments, analyzed the data, and wrote the first manuscript draft. M.R.I., M.M., L.N., and D. Manganaro performed part of the experiments. E.M. and A.C. analyzed the proteomics data, and S.J. the transcriptomics data. D.P. designed the native ChIP H4R3me2a experiments. D. Musiani and T.B. designed the research project. T.B. supervised the experiments and wrote and edited the manuscript. All authors read and approved the final manuscript.

DECLARATION OF INTERESTS

The authors declare no competing interests.

Received: October 11, 2018
Revised: August 2, 2019
Accepted: December 17, 2019
Published: January 28, 2020

REFERENCES

Adamson, B., Smogorzewska, A., Sigoillot, F.D., King, R.W., and Elledge, S.J. (2012). A genome-wide homologous recombination screen identifies the RNA-binding protein RBMX as a component of the DNA-damage response. Nat. Cell Biol. *14*, 318–328.

Altan, B., Yokobori, T., Ide, M., Mochiki, E., Toyomasu, Y., Kogure, N., Kimura, A., Hara, K., Bai, T., Bao, P., et al. (2016). Nuclear PRMT1 expression is associated with poor prognosis and chemosensitivity in gastric cancer patients. Gastric Cancer *19*, 789–797.

Bao, X., Siprashvili, Z., Zarnegar, B.J., Shenoy, R.M., Rios, E.J., Nady, N., Qu, K., Mah, A., Webster, D.E., Rubin, A.J., et al. (2017). CSNK1a1 Regulates PRMT1 to Maintain the Progenitor State in Self-Renewing Somatic Tissue. Dev Cell *43*, 227–239.e5.

Batth, T.S., Francavilla, C., and Olsen, J.V. (2014). Off-line high-pH reversed-phase fractionation for in-depth phosphoproteomics. J. Proteome Res. *13*, 6176–6186.

Bedford, M.T., and Clarke, S.G. (2009). Protein arginine methylation in mammals: who, what, and why. Mol. Cell *33*, 1–13.

Bedford, M.T., and Richard, S. (2005). Arginine methylation an emerging regulator of protein function. Mol. Cell *18*, 263–272.

Blanc, R.S., and Richard, S. (2017). Arginine Methylation: The Coming of Age. Mol. Cell *65*, 8–24.

Boisvert, F.M., Déry, U., Masson, J.Y., and Richard, S. (2005). Arginine methylation of MRE11 by PRMT1 is required for DNA damage checkpoint control. Genes Dev. *19*, 671–676.

Bremang, M., Cuomo, A., Agresta, A.M., Stugiewicz, M., Spadotto, V., and Bonaldi, T. (2013). Mass spectrometry-based identification and characterisation of lysine and arginine methylation in the human proteome. Mol. Biosyst. *9*, 2231–2247.

Bruzzone, M., Centurioni, M.G., Giglione, P., Gualco, M., Merlo, D.F., Miglietta, L., Cosso, M., Giannelli, F., Cristoforoni, P., and Ferrarini, M. (2011). Second-line treatment with intravenous gemcitabine and oral etoposide in platinum-resistant advanced ovarian cancer patients: results of a phase II study. Oncology *80*, 238–246.

Cheung, N., Fung, T.K., Zeisig, B.B., Holmes, K., Rane, J.K., Mowen, K.A., Finn, M.G., Lenhard, B., Chan, L.C., and So, C.W. (2016). Targeting Aberrant Epigenetic Networks Mediated by PRMT1 and KDM4C in Acute Myeloid Leukemia. Cancer Cell *29*, 32–48.

Coppé, J.P., Patil, C.K., Rodier, F., Sun, Y., Muñoz, D.P., Goldstein, J., Nelson, P.S., Desprez, P.Y., and Campisi, J. (2008). Senescence-associated secretory phenotypes reveal cell-nonautonomous functions of oncogenic RAS and the p53 tumor suppressor. PLoS Biol. *6*, 2853–2868.

Coppé, J.P., Desprez, P.Y., Krtolica, A., and Campisi, J. (2010). The senescence-associated secretory phenotype: the dark side of tumor suppression. Annu. Rev. Pathol. *5*, 99–118.

Côté, J., Boisvert, F.M., Boulanger, M.C., Bedford, M.T., and Richard, S. (2003). Sam68 RNA binding protein is an in vivo substrate for protein arginine N-methyltransferase 1. Mol. Biol. Cell *14*, 274–287.

Cox, J., and Mann, M. (2008). MaxQuant enables high peptide identification rates, individualized p.p.b.-range mass accuracies and proteome-wide protein quantification. Nat. Biotechnol. *26*, 1367–1372.

Cox, J., Neuhauser, N., Michalski, A., Scheltema, R.A., Olsen, J.V., and Mann, M. (2011). Andromeda: a peptide search engine integrated into the MaxQuant environment. J. Proteome Res. *10*, 1794–1805.

Cox, J., Hein, M.Y., Luber, C.A., Paron, I., Nagaraj, N., and Mann, M. (2014). Accurate proteome-wide label-free quantification by delayed normalization and maximal peptide ratio extraction, termed MaxLFQ. Mol. Cell. Proteomics *13*, 2513–2526.

Davalos, A.R., Coppe, J.P., Campisi, J., and Desprez, P.Y. (2010). Senescent cells as a source of inflammatory factors for tumor progression. Cancer Metastasis Rev. *29*, 273–283.

Deminoff, S.J., Howard, S.C., Hester, A., Warner, S., and Herman, P.K. (2006). Using substrate-binding variants of the cAMP-dependent protein kinase to identify novel targets and a kinase domain important for substrate interactions in Saccharomyces cerevisiae. Genetics *173*, 1909–1917.

Dhar, S., Vemulapalli, V., Patananan, A.N., Huang, G.L., Di Lorenzo, A., Richard, S., Comb, M.J., Guo, A., Clarke, S.G., and Bedford, M.T. (2013). Loss of the major Type I arginine methyltransferase PRMT1 causes substrate scavenging by other PRMTs. Sci. Rep. *3*, 1311.

Eram, M.S., Shen, Y., Szewczyk, M., Wu, H., Senisterra, G., Li, F., Butler, K.V., Kaniskan, H.U., Speed, B.A., Dela Seña, C., et al. (2016). A Potent, Selective, and Cell-Active Inhibitor of Human Type I Protein Arginine Methyltransferases. ACS Chem. Biol. *11*, 772–781.

Ferrari, K.J., Scelfo, A., Jammula, S., Cuomo, A., Barozzi, I., Stützer, A., Fischle, W., Bonaldi, T., and Pasini, D. (2014). Polycomb-dependent H3K27me1 and H3K27me2 regulate active transcription and enhancer fidelity. Mol. Cell *53*, 49–62.

Freund, A., Patil, C.K., and Campisi, J. (2011). p38MAPK is a novel DNA damage response-independent regulator of the senescence-associated secretory phenotype. EMBO J. *30*, 1536–1548.

Gentile, M., Latonen, L., and Laiho, M. (2003). Cell cycle arrest and apoptosis provoked by UV radiation-induced DNA damage are transcriptionally highly divergent responses. Nucleic Acids Res. *31*, 4779–4790.

Goulet, I., Gauvin, G., Boisvenue, S., and Côté, J. (2007). Alternative splicing yields protein arginine methyltransferase 1 isoforms with distinct activity, substrate specificity, and subcellular localization. J. Biol. Chem. *282*, 33009–33021.

Guccione, E., and Richard, S. (2019). The regulation, functions and clinical relevance of arginine methylation. Nat. Rev. Mol. Cell Biol. *20*, 642–657.

Guil, S., Long, J.C., and Cáceres, J.F. (2006). hnRNP A1 relocalization to the stress granules reflects a role in the stress response. Mol. Cell. Biol. *26*, 5744–5758.

Hassa, P.O., Covic, M., Bedford, M.T., and Hottiger, M.O. (2008). Protein arginine methyltransferase 1 coactivates NF-kappaB-dependent gene expression synergistically with CARM1 and PARP1. J. Mol. Biol. *377*, 668–678.

Henao-Mejia, J., and He, J.J. (2009). Sam68 relocalization into stress granules in response to oxidative stress through complexing with TIA-1. Exp. Cell Res. *315*, 3381–3395.

Herrmann, F., Lee, J., Bedford, M.T., and Fackelmayer, F.O. (2005). Dynamics of human protein arginine methyltransferase 1(PRMT1) in vivo. J. Biol. Chem. *280*, 38005–38010.

Hornbeck, P.V., Zhang, B., Murray, B., Kornhauser, J.M., Latham, V., and Skrzypek, E. (2015). PhosphoSitePlus, 2014: mutations, PTMs and recalibrations. Nucleic Acids Res. *43*, D512–D520.

Huang da, W., Sherman, B.T., and Lempicki, R.A. (2009). Systematic and integrative analysis of large gene lists using DAVID bioinformatics resources. Nat. Protoc. *4*, 44–57.

Huxford, T., and Ghosh, G. (2009). A structural guide to proteins of the NF-kappaB signaling module. Cold Spring Harb. Perspect. Biol. *1*, a000075.

Iliuk, A., Liu, X.S., Xue, L., Liu, X., and Tao, W.A. (2012). Chemical visualization of phosphoproteomes on membrane. Mol. Cell. Proteomics *11*, 629–639.

Kedersha, N., Ivanov, P., and Anderson, P. (2013). Stress granules and cell signaling: more than just a passing phase? Trends Biochem. Sci. *38*, 494–506.

Kim, D., Langmead, B., and Salzberg, S.L. (2015). HISAT: a fast spliced aligner with low memory requirements. Nat. Methods *12*, 357–360.

Kim, J.H., Yoo, B.C., Yang, W.S., Kim, E., Hong, S., and Cho, J.Y. (2016). The Role of Protein Arginine Methyltransferases in Inflammatory Responses. Mediators Inflamm. *2016*, 4028353.

Larsen, S.C., Sylvestersen, K.B., Mund, A., Lyon, D., Mullari, M., Madsen, M.V., Daniel, J.A., Jensen, L.J., and Nielsen, M.L. (2016). Proteome-wide analysis of arginine monomethylation reveals widespread occurrence in human cells. Sci. Signal. *9*, rs9.

Love, M.I., Huber, W., and Anders, S. (2014). Moderated estimation of fold change and dispersion for RNA-seq data with DESeq2. Genome Biol. *15*, 550.

Maddelein, D., Colaert, N., Buchanan, I., Hulstaert, N., Gevaert, K., and Martens, L. (2015). The iceLogo web server and SOAP service for determining protein consensus sequences. Nucleic Acids Res. *43* (*W1*), W543–W546.

Maguire, O., Collins, C., O'Loughlin, K., Miecznikowski, J., and Minderman, H. (2011). Quantifying nuclear p65 as a parameter for NF-κB activation: Correlation between ImageStream cytometry, microscopy, and Western blot. Cytometry A *79*, 461–469.

Massignani, E., Cuomo, A., Musiani, D., Jammula, S., Pavesi, G., and Bonaldi, T. (2019). hmSEEKER: Identification of hmSILAC Doublets in MaxQuant Output Data. Proteomics *19*, e1800300.

Matsuki, H., Takahashi, M., Higuchi, M., Makokha, G.N., Oie, M., and Fujii, M. (2013). Both G3BP1 and G3BP2 contribute to stress granule formation. Genes Cells *18*, 135–146.

Méndez, J., and Stillman, B. (2000). Chromatin association of human origin recognition complex, cdc6, and minichromosome maintenance proteins during the cell cycle: assembly of prereplication complexes in late mitosis. Mol. Cell. Biol. *20*, 8602–8612.

Musiani, D., Bok, J., Massignani, E., Wu, L., Tabaglio, T., Ippolito, M.R., Cuomo, A., Ozbek, U., Zorgati, H., Ghoshdastider, U., et al. (2019). Proteomics profiling of arginine methylation defines PRMT5 substrate specificity. Sci. Signal. *12*, eaat8388.

Ong, S.E., Mittler, G., and Mann, M. (2004). Identifying and quantifying in vivo methylation sites by heavy methyl SILAC. Nat. Methods *1*, 119–126.

Rappsilber, J., Mann, M., and Ishihama, Y. (2007). Protocol for micro-purification, enrichment, pre-fractionation and storage of peptides for proteomics using StageTips. Nat. Protoc. *2*, 1896–1906.

Reintjes, A., Fuchs, J.E., Kremser, L., Lindner, H.H., Liedl, K.R., Huber, L.A., and Valovka, T. (2016). Asymmetric arginine dimethylation of RelA provides a repressive mark to modulate TNFα/NF-κB response. Proc. Natl. Acad. Sci. USA *113*, 4326–4331.

Rust, H.L., Subramanian, V., West, G.M., Young, D.D., Schultz, P.G., and Thompson, P.R. (2014). Using unnatural amino acid mutagenesis to probe the regulation of PRMT1. ACS Chem. Biol. *9*, 649–655.

Sabatel, H., Pirlot, C., Piette, J., and Habraken, Y. (2011). Importance of PIKKs in NF-κB activation by genotoxic stress. Biochem. Pharmacol. *82*, 1371–1383.

Salama, R., Sadaie, M., Hoare, M., and Narita, M. (2014). Cellular senescence and its effector programs. Genes Dev. *28*, 99–114.

Salminen, A., Ojala, J., and Kaarniranta, K. (2011). Apoptosis and aging: increased resistance to apoptosis enhances the aging process. Cell. Mol. Life Sci. *68*, 1021–1031.

Salminen, A., Kauppinen, A., and Kaarniranta, K. (2012). Emerging role of NF-κB signaling in the induction of senescence-associated secretory phenotype (SASP). Cell. Signal. *24*, 835–845.

Schindelin, J., Arganda-Carreras, I., Frise, E., Kaynig, V., Longair, M., Pietzsch, T., Preibisch, S., Rueden, C., Saalfeld, S., Schmid, B., Tinevez, J., Y.., et al. (2012). Fiji: an open-source platform for biological-image analysis. Nat Methods *28*, 676–682.

Shevchenko, A., Tomas, H., Havlis, J., Olsen, J.V., and Mann, M. (2006). In-gel digestion for mass spectrometric characterization of proteins and proteomes. Nat. Protoc. *1*, 2856–2860.

Snel, B., Lehmann, G., Bork, P., and Huynen, M.A. (2000). STRING: a web-server to retrieve and display the repeatedly occurring neighbourhood of a gene. Nucleic Acids Res. *28*, 3442–3444.

Soldi, M., and Bonaldi, T. (2013). The proteomic investigation of chromatin functional domains reveals novel synergisms among distinct heterochromatin components. Mol. Cell. Proteomics *12*, 764–780.

Soldi, M., and Bonaldi, T. (2014). The ChroP approach combines ChIP and mass spectrometry to dissect locus-specific proteomic landscapes of chromatin. J. Vis. Exp. (*86*), e51220.

Soldi, M., Cuomo, A., and Bonaldi, T. (2014). Improved bottom-up strategy to efficiently separate hypermodified histone peptides through ultra-HPLC separation on a bench top Orbitrap instrument. Proteomics *14*, 2212–2225.

Su, G., Morris, J.H., Demchak, B., and Bader, G.D. (2014). Biological network exploration with Cytoscape 3. Curr. Protoc. Bioinformatics *47*, 8.13.1–8.13.24.

Sun, X., Shi, B., Zheng, H., Min, L., Yang, J., Li, X., Liao, X., Huang, W., Zhang, M., Xu, S., et al. (2018). Senescence-associated secretory factors induced by cisplatin in melanoma cells promote non-senescent melanoma cell growth through activation of the ERK1/2-RSK1 pathway. Cell Death Dis. *9*, 260.

Sylvestersen, K.B., Horn, H., Jungmichel, S., Jensen, L.J., and Nielsen, M.L. (2014). Proteomic analysis of arginine methylation sites in human cells reveals dynamic regulation during transcriptional arrest. Mol. Cell. Proteomics *13*, 2072–2088.

Takai, H., Masuda, K., Sato, T., Sakaguchi, Y., Suzuki, T., Suzuki, T., Koyama-Nasu, R., Nasu-Nishimura, Y., Katou, Y., Ogawa, H., et al. (2014). 5-Hydroxymethylcytosine plays a critical role in glioblastomagenesis by recruiting the CHTOP-methylosome complex. Cell Rep. *9*, 48–60.

Tang, J., Frankel, A., Cook, R.J., Kim, S., Paik, W.K., Williams, K.R., Clarke, S., and Herschman, H.R. (2000). PRMT1 is the predominant type I protein arginine methyltransferase in mammalian cells. J. Biol. Chem. *275*, 7723–7730.

Thandapani, P., O'Connor, T.R., Bailey, T.L., and Richard, S. (2013). Defining the RGG/RG motif. Mol. Cell *50*, 613–623.

Thomas, M.G., Loschi, M., Desbats, M.A., and Boccaccio, G.L. (2011). RNA granules: the good, the bad and the ugly. Cell. Signal. *23*, 324–334.

Tsai, W.C., Gayatri, S., Reineke, L.C., Sbardella, G., Bedford, M.T., and Lloyd, R.E. (2016). Arginine Demethylation of G3BP1 Promotes Stress Granule Assembly. J. Biol. Chem. *291*, 22671–22685.

Tyanova, S., Temu, T., Sinitcyn, P., Carlson, A., Hein, M.Y., Geiger, T., Mann, M., and Cox, J. (2016). The Perseus computational platform for comprehensive analysis of (prote)omics data. Nat. Methods *13*, 731–740.

Vermeulen, M., Eberl, H.C., Matarese, F., Marks, H., Denissov, S., Butter, F., Lee, K.K., Olsen, J.V., Hyman, A.A., Stunnenberg, H.G., and Mann, M. (2010). Quantitative interaction proteomics and genome-wide profiling of epigenetic histone marks and their readers. Cell *142*, 967–980.

Wada, K., Inoue, K., and Hagiwara, M. (2002). Identification of methylated proteins by protein arginine N-methyltransferase 1, PRMT1, with a new expression cloning strategy. Biochim. Biophys. Acta *1591*, 1–10.

Wang, H., Huang, Z.Q., Xia, L., Feng, Q., Erdjument-Bromage, H., Strahl, B.D., Briggs, S.D., Allis, C.D., Wong, J., Tempst, P., and Zhang, Y. (2001). Methylation of histone H4 at arginine 3 facilitating transcriptional activation by nuclear hormone receptor. Science *293*, 853–857.

Wang, Q., Wang, K., and Ye, M. (2017). Strategies for large-scale analysis of non-histone protein methylation by LC-MS/MS. Analyst (Lond.) *142*, 3536–3548.

Willmore, E., de Caux, S., Sunter, N.J., Tilby, M.J., Jackson, G.H., Austin, C.A., and Durkacz, B.W. (2004). A novel DNA-dependent protein kinase inhibitor, NU7026, potentiates the cytotoxicity of topoisomerase II poisons used in the treatment of leukemia. Blood *103*, 4659–4665.

Yu, Z., Chen, T., Hébert, J., Li, E., and Richard, S. (2009). A mouse PRMT1 null allele defines an essential role for arginine methylation in genome maintenance and cell proliferation. Mol. Cell. Biol. *29*, 2982–2996.

Yu, Z., Vogel, G., Coulombe, Y., Dubeau, D., Spehalski, E., Hébert, J., Ferguson, D.O., Masson, J.Y., and Richard, S. (2012). The MRE11 GAR motif regulates DNA double-strand break processing and ATR activation. Cell Res. *22*, 305–320.

Zhao, Y., Lu, Q., Li, C., Wang, X., Jiang, L., Huang, L., Wang, C., and Chen, H. (2019). PRMT1 regulates the tumour-initiating properties of esophageal squamous cell carcinoma through histone H4 arginine methylation coupled with transcriptional activation. Cell Death Dis. *10*, 359.

STAR★METHODS

KEY RESOURCES TABLE

REAGENT or RESOURCE	SOURCE	IDENTIFIER
Antibodies		
anti-Lamin B1	Abcam	Cat#ab16048; RRID:AB_443298
anti-Phospho-Ser139 H2A.x	Abcam	Cat#ab2893; RRID:AB_303388
anti-DNA-PK	Abcam	Cat#ab70250; RRID:AB_1209452
anti-Phospho-DNA-PK S2056	Abcam	Cat#ab18192; RRID:AB_869495
anti-PRMT1	Abcam	Cat#ab73246; RRID:AB_1640800
anti-PRMT1 ChIP grade	Abcam	Cat#ab3768; RRID:AB_304062
anti-GAPDH	Abcam	Cat#ab8245; RRID:AB_2107448
anti-H3R17me2a	Abcam	Cat#ab8284; RRID:AB_306434
anti-H3R2me2a	Abcam	Cat#ab194706; RRID:AB_2819356
anti-Histone H3	Abcam	Cat#ab1791; RRID:AB_302613
anti-Histone H4	Abcam	Cat#ab7311; RRID:AB_305837
anti-Phospho-(Ser-Threo)	Cell Signaling Technology	Cat#9631; RRID:AB_330308
anti-NF-kB p65	Cell Signaling Technology	Cat#8242; RRID:AB_10859369
anti-NF-kB p65 C20	Santa Cruz Biotechnology	Cat#sc-372; RRID:AB_632037
anti-vinculin	Sigma-Aldrich	Cat# V9131; RRID:AB_477629
anti-H4R3me2a	Active Motif	Cat#39705; RRID:AB_2793313
anti-rabbit IgG, HRP-linked	Cell Signaling Technology	Cat#7074; RRID:AB_2099233
anti-mouse IgG, HRP-linked	Cell Signaling Technology	Cat#7076; RRID:AB_330924
Alexa 488 anti-Rabbit	Thermo Fisher Scientific	Cat#A21206; RRID:AB_141708
anti-rabbit IgG	Merck	Cat#12-370; RRID:AB_145841
anti-Tubulin	Merck	Cat#T9026; RRID:AB_477593
anti-PSP1	Bethyl Laboratories	Cat#A303-205A; RRID:AB_10952866
anti-DDX17	Abcam	Cat#AB71958; RRID:AB_1268477
Bacterial and Virus Strains		
pLKO.1	Thermo Fisher Scientific	SHCLND
Chemicals, Peptides, and Recombinant Proteins		
Cisplatin (CDDP)	In house produced	N/A
Gemcitabine (GEM)	In house produced	N/A
Hydroxyurea (HU)	Sigma Aldrich	Cat#H8627
MS023	Structural Genomic Consortium	N/A
MS094	Structural Genomic Consortium	N/A
NU7026	Selleckchem	Cat#S2893
BAY-117085	Merck Millipore	Cat#B5681
Benzonase	Millipore Merck	Cat#1.01654.0001
Human PRMT1 peptide	Abcam	Cat#ab73687
Sequencing Grade Modified Trypsin	Promega	Cat#V5113
Nuclease S7 Micrococcal nuclease, from *Staphylococcus aureus*	Merck	Cat#10107921001
APC-conjugated Annexin V	Thermo Fisher Scientific	Cat#A35110
Critical Commercial Assays		
NuPAGE 4-12% Bis-Tris Protein Gels	Thermo Fisher Scientific	Cat#NP0335BOX
BCA Assay Kit	Thermo Fisher Scientific	Cat#23225
Clarity Western ECL Substrate	Bio-rad	Cat#1705061

(*Continued on next page*)

Continued

REAGENT or RESOURCE	SOURCE	IDENTIFIER
Dynabeads Protein G for Immunoprecipitation	Thermo Fisher Scientific	Cat#10003D
Colloidal Coomassie staining Instant Blue	Sigma Aldrich	Cat#ISB1L-1L
LDS sample Buffer	Thermo Fisher Scientific	Cat#NP0007
Sep-Pak C18 cartridges	Waters	Cat#186000308
PTMScan® Asymmetric Di-Methyl Arginine Motif [adme-R] Kit	Cell Signaling Technology	Cat#13474
PTMScan® Mono-Methyl Arginine Motif [mme-RG] Kit	Cell Signaling Technology	Cat#12235
Quick-RNA Miniprep kit	Zymo research	Cat#R1055
ImProm-II Reverse Transcriptase	Promega	Cat#A3801
Fast SYBR™ Green Master mix	Thermo Fisher Scientific	Cat#4385614
QIAquick PCR Purification Kit	QIAGEN	Cat#28104
Protein G Sepharose 4 Fast Flow antibody purification resin	GE Healthcare Life Sciences	Cat#17061801
Bead-based immunoassays	BD BioSciences	Cat#170116
Crystal violet solution	Sigma Aldrich	Cat#V5265
Deposited Data		
MS-proteomics data	This paper	ProteomeXchange Database: PXD014799
RNA-seq data	This paper	GEO Database: GSE106609
Experimental Models: Cell Lines		
SK-OV-3	ATCC	HTB-77™
HeLa	ATCC	CCL-2
HEK293T	DMSZ	ACC 635
Oligonucleotides		
IL6 gene expression Fwd; 5′-CCAGAGCTGTGCAGATGAGT-3′	This paper	N/A
IL6 gene expression Rev; 5′-ATTTGTGGTTGGGTCAGGGG-3′	This paper	N/A
IL1a gene expression Fwd; 5′-AGGTTCTGAAGAAGAGACGGT-3′	This paper	N/A
IL1a gene expression Rev; 5′-GGTGCTGACCTAGGCTTGAT-3′	This paper	N/A
IL1b gene expression Fwd; 5′-CTCTTCAGCCAATCTTCATTGC-3′	This paper	N/A
IL1b gene expression Rev; 5′-GAACAAGTCATCCTCATTGCCA-3′	This paper	N/A
IL8 gene expression Fwd; 5′-CTTGGCAGCCTTCCTGATTTCT-3′	This paper	N/A
IL8 gene expression Rev; 5′-GTTTTCCTTGGGGTCCAGACAG-3′	This paper	N/A
TNF*a* gene expression Fwd; 5′-ACTTTGGAGTGATCGGCCC-3′	This paper	N/A
TNF*a* gene expression Rev; 5′-CATTGGCCAGGAGGGCATT-3′	This paper	N/A
IL6 promoter Fwd; 5′-ATGTGGGATTTTCCCATGAGTC-3′	This paper	N/A
IL6 promoter Rev; 5′-GCCTCAGACATCTCCAGTCCTA-3′	This paper	N/A
IL8 promoter Fwd; 5′-TTGAAGCCCTCCTATTCCT-3′	This paper	N/A

(*Continued on next page*)

Continued

REAGENT or RESOURCE	SOURCE	IDENTIFIER
IL8 promoter Rev; 5′-AAGGACTGACTATATAGCAG-3′	This paper	N/A
IL1a promoter Fwd; 5′-ACTCCAACTGGGAACCCAAA-3′	This paper	N/A
IL1a promoter Rev; 5′-CTGTGGCCAGCCTAGTTCAG-3′	This paper	N/A
IL1b promoter Fwd; 5′-GTGTCTTCCACTTTGTCCCACAT-3′	This paper	N/A
IL1b promoter Rev; 5′-TGACAATCGTTGTGCAGTTGATG-3′	This paper	N/A
shRNA PRMT1 sh#1; 5′-CCGGCAGTACAAAGACTACAA-3′	This paper	N/A
shRNA PRMT1 sh#3; 5′-GTGTTCCAGTATCTCTGATTA-3′	This paper	N/A
shRNA DNA-PK; 5′-GATCGCACCTTACTCTGTT-3′	This paper	N/A
Software and Algorithms		
MaxQuant software	Cox et al., 2014	https://maxquant.org/
Andromeda search engine	Cox and Mann, 2008; Cox et al., 2011	https://www.maxquant.org/maxquant/
Perseus	Tyanova et al., 2016	https://www.maxquant.org/perseus/
STRING	Snel et al., 2000	https://string-db.org/
Cytoscape 3.0	Su et al., 2014	https://cytoscape.org/cy3.html
hmSEEKER	Massignani et al., 2019	N/A
hmLINKER	Musiani et al., 2019	N/A
iceLogo web application	Maddelein et al., 2015	https://iomics.ugent.be/icelogoserver/
PhosphoSite Plus database	Hornbeck et al., 2015	https://www.phosphosite.org/homeAction.action
Nuclear/cytoplasmic ratio IF images quantification	In this paper	N/A
DESeq2	Love et al., 2014	https://bioconductor.org/packages/release/bioc/html/DESeq2.html
DAVID	Huang da et al., 2009	https://david.ncifcrf.gov/
ImageJ plugin “analyse particles”	ImageJ	https://imagej.nih.gov/ij/download.html

LEAD CONTACT AND MATERIALS AVAILABILITY

Further information and requests for resources and reagents should be directed to and will be fulfilled by the Lead Contact, Tiziana Bonaldi (tiziana.bonaldi@ieo.it). All plasmids generated in this study will be made available on request and may require a completed Materials Transfer Agreement if there is potential for commercial application.

EXPERIMENTAL MODEL AND SUBJECT DETAILS

Cell culture conditions and reagents

SK-OV-3 cell line derived from a serous ovarian carcinoma was purchased from the American Type Culture Collection (ATCC, Manassas, VA, USA) in 2011. SK-OV-3 cells were cultured in RPMI 1640 supplemented with 10% Fetal Bovine Serum (FBS, Life Technologies), 1% glutamine, 100 U/ml penicillin,100 mg/ml streptomycin and cultured at 37°C in a 5% CO2 humidified atmosphere. HeLa derived from cervix adeno carcinoma were purchased from ATCC. HEK293T derived from embryonal kidney were purchased from DMSZ. The cell lines were authenticated by short tandem repeat (STR) analysis using the Geneprint kit of Promega (B9510). HeLa, HEK293T cell lines were grown in DMEM with glutamine, 10% FBS and antibiotics. All the cell lines were tested free of mycoplasma contamination. Cisplatin (CDDP) and gemcitabine (GEM) were obtained from the hospital pharmacy at the European Institute of Oncology (Milan, Italy), while hydroxyurea (HU 2mM; H8627) was purchased from Sigma Aldrich. MS023 (10 μM) and its inactive structural analog MS094 (10 μM) were provided by Structural Genomic Consortium (SGC, University of Toronto, Toronto, Ontario, Canada). NU7026 (DNA-PKi; S2893) inhibitor was purchased from Selleckchem. CDDP was used at a concentration of

20 μM for SK-OV-3 and 10 μM for HeLa cells, if not otherwise indicated. All the other compounds were used at the indicated doses. Cells were exposed to UVC (254 nm) at a dose of 40 J/m^2 using a Stratalinker 2400 UV cross-linker (Stratagene, La Jolla, CA) and to ionizing radiation IR (10Gy) generated by a high-voltage X-ray-generator tube (Faxitron X-Ray Corporation).

METHOD DETAILS

SILAC and heavy methyl SILAC cell culture conditions

For SILAC, SK-OV-3 were grown in ''Light'', ''Medium'' and ''Heavy'' SILAC RPMI (Thermo Fisher Scientific, # 89984), supplemented with either L-Arginine, L-Lysine or their medium (Arg: Sigma-Aldrich, 643440; Lys: Sigma-Aldrich, 616192) or heavy (Arg: Sigma-Aldrich, 608033; Lys: Sigma-Aldrich, 608041) isotope-counterparts. Arginine and Lysine were added at a concentration of 84 mg/L and 146 mg/L, respectively. The SILAC media were then supplemented with 10% dialyzed FBS (GIBCO, Life Technologies 26400-044), 1% glutamine, 100 U/ml Penicillin and 100 mg/ml Streptomycin.

For hmSILAC, SK-OV-3 cells were cultured in ''Light'' and ''Heavy'' hmSILAC RPMI media (PAA, custom) supplemented with L-Arginine (Sigma-Aldrich, A6969) L-Lysine (Sigma-Aldrich, L8662), plus either L-[$^{13}CD_3$]-Methionine (Met-4, heavy, Sigma-Aldrich, 299154) or L-[$^{12}CH_3$]-methionine (Met-0, light, Sigma-Aldrich, M5308), respectively. Concentration of L-Methionine was 30 mg/L. The hmSILAC media were then supplemented with 10% dialyzed FBS (GIBCO, Life Technologies 26400-044), 1% glutamine, 100 U/ml Penicillin and 100 mg/ml Streptomycin.

Both SILAC and hmSILAC SK-OV-3 cells were grown in the respective heavy-isotopes containing media for at least 9 replication cycles to ensure full incorporation, with a careful monitoring of growth rate, viability and overall morphology, to guarantee that normal physiology was preserved.

Vectors and infections

Viral particles for the generation of the knockdown cell lines used in this study were produced as previously described (24903273). The following sequences of the shRNA were used for PRMT1 and DNA-PK knockdown, respectively: 5′-CCGGCAGTACAAAGAC TACAA-3′ (sh#1, PRMT1), 5′-GTGTTCCAGTATCTCTGATTA-3′ (sh#3, PRMT1), 5′- GATCGCACCTTACTCTGTT −3′ (shDNA-PK). All the shRNA sequences were cloned into pLKO.1 vector to generate the knockdown cell lines.

Cell lysis, sub-cellular fractionation and Western Blot analysis

For whole cell lysis, harvested cell culture pellets were rinsed with PBS, lysed in SDS-containing Buffer (4.8% SDS, 20% glycerol, 0.1 M Tris-HCl, pH 7.5) and sonicated. Protein lysates were centrifuged at maximum speed for 10 min.

For sub-cellular fractionation into cytosol, nucleosol and chromatin compartments, cell lysates were obtained according to the protocol described in Méndez and Stillman (2000). Briefly, cells were resuspended at a concentration of 4 × 10^7cells/ml in Buffer A (10 mM HEPES, [pH 7.9], 10 mM KCl, 1.5 mM $MgCl_2$, 0.34 M sucrose, 10% glycerol, 1 mM DTT and 1X Roche Protease Inhibitors). Cytosolic fractions were obtained incubating the cells for 5 min on ice upon addition of Triton X-100 (0.1%) to Buffer A, followed by low-speed centrifugation (4 min, 1,300 × g, 4°C). The cytosolic fraction (supernatant) was further clarified by high-speed centrifugation (15 min, 20,000 × g, 4°C) to remove cell debris and insoluble aggregates. Nuclei (pellets) were washed once in Buffer A and then lysed in Buffer B (3 mM EDTA, 0.2 mM EGTA, 1 mM DTT, 1X Roche Protease Inhibitors as described above) for 30 min at 4°C. Insoluble chromatin was collected by centrifugation (4 min, 1,700 × g, 4°C), washed once in Buffer B, and centrifuged again under the same conditions. The final chromatin pellet was resuspended in SDS-containing Buffer and sonicated for 10 s. Alternatively, for the immuno-purification of proteins from the chromatin fraction, after the wash in Buffer B the chromatin pellet was resuspended in 2 volumes of Buffer C420 (420 mM NaCl; 20 mM HEPES KOH pH 7.9; 1.5 mM $MgCl_2$; 0.2 mM EDTA; 0.1% NP-40; 0.5 mM DTT) and rocked for 30 min at 4°C. Subsequently, the NaCl concentration was reduced to 150 mM, and 50U of Benzonase (1.01654.0001 Millipore Merck) was added to each extract and incubated for 15 min at 37°C to release the chromatin-associated proteins. Finally, the lysates were centrifuged for 1h at 13000 x g at 4°C for 1 h and the chromatin proteins were collected and quantified.

For the preparation of cytoplasmic and nuclear extracts, cell pellets were processed according to a slightly modified version of a previously published protocol (Vermeulen et al., 2010). Briefly, cells were harvested, washed once with PBS and resuspended in 2 volumes of Lysis Buffer A (10 mM HEPES-KOH pH 7.9, 1.5 mM MgCl2, 10 mM KCl, 0.2% NP-40, 1X Roche Protease Inhibitors, 1U/μL NEB RNase Inhibitors) and left for 10 min on ice. After 40 strokes with a dounce homogenizer, cells were centrifuged 15 min at 3750 rpm. The supernatant (representing the cytoplasmic extract) was collected and the pellet (corresponding to crude nuclei) was washed twice with PBS and re-suspended in 2 volumes of Buffer C (420 mM NaCl, 0.1% NP40, 0.5 mM DTT, 20 mM HEPES-KOH pH 7.9, 2 mM MgCl2, 0.2 mM EDTA and 20% glycerol, 1X Roche Protease Inhibitors, 1U/μl NEB RNase Inhibitors). The suspension was rocked 1h at 4°C to extract proteins by high-salt extraction and afterward diluted with Buffer C without NaCl to reduce the NaCl to a final concentration of 150 mM. The nuclear extract was then treated with 125U of Benzonase (Sigma Aldrich) for 30 min at 37°C in a thermo-mixer at 900 rpm to digest the nucleic acids and release all the chromatin associated protein and finally ultracentrifuged at 33000 rpm for 1h. The supernatant representing the nuclear extract was collected and quantified.

Protein extracts from total, cytosolic, nuclear and chromatin-enriched lysates were quantified using BCA (Pierce BCA Protein assay kit, 23225) and equal amounts of proteins were resolved by SDS-PAGE electrophoresis and blotted on Transfer membrane

(Immobilon-P, Merck Millipore IPVH00010). Membrane blocking (10% BSA/TBS 0.2% Tween-20 for 30 min at RT) was followed by incubation with the appropriate primary antibodies and HRP-conjugated secondary antibodies (Cell Signaling Technology). Proteins were detected by ECL (Bio-Rad). The following primary antibodies were used: Lamin B1 (ab16048), phospho-Ser139 H2A.x (ab2893), DNA-PK (ab70250), phospho-DNA-PK S2056 (ab18192), PRMT1 (ab73246, ab3768), GAPDH (ab8245), H3R17me2a (ab8284), H3R2me2a (ab194706), histone H3 (ab1791), histone H4 (ab7311) were purchased from Abcam; Phospho-(Ser-Threo) (CST, #9631), NF-kB p65 (CST, #8242) were purchased from Cell Signaling Technology; vinculin (06-866) from Merck Millipore; H4R3me2a (#39705) was purchased from Active Motif; NF-kB p65 C20 (sc-372) was purchased from Santa Cruz Biotechnology; H4R3me2a (07-213-I).

PRMT1 protein co-Immunoprecipitation (PRMT1 co-IP)

Three biological replicates of PRMT1 co-immunoprecipitation (PRMT1 co-IP) were performed, each using 2 mg of SK-OV-3 nuclear lysate as input, prepared as follows. Briefly, $100x10^6$ SK-OV-3 cells were harvested, washed twice with cold PBS and re-suspended in 2 volumes of Lysis Buffer A (10 mM HEPES KOH pH 7.9, 1.5 mM MgCl2, 10 mM KCl, 0.2% NP40, 1X Roche Protease Inhibitors). After 20 strokes with a dounce homogenizer, cells were centrifuged 15 min at 3750 rpm. The supernatant (cytoplasmic extract) was collected and the pellet (corresponding to crude nuclei) was washed twice with PBS and re-suspended into 2 volumes of Buffer C (420 mM NaCl, 0.1% NP40, 0.5 mM DTT, 20 mM HEPES KOH pH 7.9, 2 mM MgCl2, 0.2 mM EDTA and 20% glycerol, 1X Roche Protease Inhibitors). The suspension was rotated 1h at 4°C and then ultra-centrifuged at 33000 rpm for 1h. After dilution of Buffer C to 150 mM NaCl (IP Buffer), the lysate was rotated at 4° overnight with 5 μg of anti-PRMT1 antibody (ab73246), in presence and absence of 50-fold molar excess of the specific competing peptide (ab73687), in order to selectively evict the antigen and the co-associated proteins from the beads, which allow to discriminate specific binders from background proteins based on the protein intensity ratio measured by MS in the two channels. G-protein-coupled magnetic beads (Dynabeads, Thermo Fisher Scientific, 100.04D) were then added and incubated for 2 hours; the captured immuno-complexes were washed 4 times with the IP Buffer and incubated with LSD sample Buffer supplemented with 100 mM DTT in order to elute the immunoprecipitated proteins. Proteins were separated on 4%–12% Bis-Tris acrylamide SDS-PAGE pre-cast gels (Novex Tris-Glycine Gels, Life technologies) and visualized using Colloidal Coomassie staining (Instant Blue, Sigma Aldrich), prior to protein digestion and LC-MS/MS analysis.

PRMT1 cross-linked chromatin immunoprecipitation (PRMT1 X-ChroP)

The immuno-enrichment of PRMT1 in the context of chromatin was achieved using the X-ChroP approach, as described in Soldi and Bonaldi (2013) with minor modifications. Briefly, $100x10^6$ SK-OV-3 cells were harvested and cell pellets were cross-linked in 1% formaldehyde PBS for 20 min at room temperature to stabilize protein–DNA and protein–protein interactions. Formaldehyde was quenched by the addition of 125 mM glycine for 5 min. After four washes with cold PBS, cells were suspended in Lysis Buffer (50 mM HEPES KOH pH 7.5, 140 mM NaCl, 1 mM EDTA, 10% glycerol, 0.5% NP-40, 0.25% Triton X-100, 0.5 mM PMSF, protease inhibitors) for 10 min at 4°C. After centrifugation, nuclear pellets were washed once and then re-suspended in ChIP incubation Buffer (10 mM Tris-HCl pH 8, 100 mM NaCl, 1 mM EDTA, 0.5 mM EGTA, 0.1% sodium deoxycholate, 0.5% sodium lauroylsarcoside, 0.5 mM PMSF, protease inhibitors). Chromatin from nuclei was sonicated at 200 W for 15 min (cycles of 30 s "on" and 1 min "off" in a cooled Bioruptor (Diagenode inc. North America, USA)). After sonication, 1% Triton X-100 was added to the sonicated chromatin to pellet the cell debris. Soluble nucleosomes -contained in the soluble supernatant after 10 min centrifugation at 13,000 rpm (4°C) - were immunoprecipitated by adding 10 μg of the PRMT1 ChIP-grade antibody (ab3768), followed by G-protein-coupled magnetic beads capture for 4 hours. After 4 washes that were carried out in 10 mM Tris-HCl pH 8, 200 mM NaCl, 1 mM EDTA, 0.5 mM EGTA, 0.5 mM PMSF, protease inhibitors, LDS sample Buffer (Thermo Fisher Scientific, NP0007) was added to the beads for 25 min at 95°C to reverse the cross-linking and elute the immunoprecipitated proteins. Proteins were separated on 4%–12% Bis-Tris acrylamide SDS-PAGE pre-cast gradient gels (Thermo Fisher Scientific) and visualized using a Colloidal Coomassie staining kit (Instant Blue, Sigma Aldrich).

In-gel digestion of immunoprecipitated proteins

Processing of gel-separated proteins prior to MS analysis was carried out as previously described, with minor modifications (Shevchenko et al., 2006). Briefly, slices were cut from gels and de-stained in 50% v/v acetonitrile (ACN)/50 mM NH4HCO3. Reduction was carried out with 10mM DTT, followed by alkylation with 55 mM iodoacetamide. After each step, samples were dehydrated with 100% ethanol and quickly dried in a centrifugal evaporator (SpeedVac). Subsequently, gel pieces were washed extensively with 50 mM NH_4HCO_3 and digested with 12.5 ng/μl trypsin (Promega, V5113) overnight at 37°C. Digested peptides were extracted with Extraction Buffer (3% TFA, 30% ACN) and 100% ACN. Prior to MS, peptides are desalted and concentrated in a single step through reversed phase chromatography on micro-column C18 Stage Tips (Rappsilber et al., 2007).

Arginine methyl-peptides enrichment for LC-MS/MS analysis

Three independent SILAC based-proteomics experiments were carried out, each in two biological replicates (Forward and Reverse experiment) and named standard SILAC, triple SILAC total and triple SILAC nuclear, respectively. For the standard SILAC, equal numbers of Light and Heavy-labeled SK-OV-3 cells were mixed in a 1:1 ratio, while for the triple SILAC experiments Light, Medium and Heavy-labeled SK-OV-3 cells were mixed in a 1:1:1 ratio. For the standard SILAC and the triple SILAC total, cell pellets were lysed

in Urea Lysis Buffer (9 M urea, 20 mM HEPES pH 8.0) supplemented with 1X Roche proteases and phosphatases inhibitors, sonicated and cleared from debris by ultracentrifugation (20.000 x *g* for 15 min at 15°C). For the triple SILAC nuclear experiment, cell pellets were resuspended in Buffer A (10 mM HEPES [pH 7.9], 10 mM KCl, 1.5 mM $MgCl_2$, 0.34 M sucrose, 10% glycerol, 0.1% Triton X-100, 1 mM DTT and 1X Roche Protease Inhibitors) for 5 min on ice, followed by low-speed centrifugation (4 min, 1,300 × g, 4°C) to separate the cytosolic fractions (supernatant) from the nuclei (pellets). Nuclei were then washed twice in Buffer A without Triton X-100 and lysed in Urea Lysis Buffer supplemented with 1X Roche proteases and phosphatases inhibitors, sonicated and cleared by ultracentrifugation (20.000 x *g* for 15 min at 15°C). For in-solution digestion, 20/50 mg of proteins were reduced by adding 4.5 mM DTT (Sigma-Aldrich) for 30 min at 55°C, alkylated with 5.5 mM iodoacetamide (IAA: 10% v/v for 15 min at room temperature in the dark, Sigma Aldrich) and digested overnight with sequencing grade trypsin (1:100 w/w, Promega) after a four-fold dilution in 25 mM ammonium bicarbonate solution. Protease digestion was terminated by the addition of trifluoroacetic acid (TFA) to pH < 3. Precipitated material was removed by centrifugation for 15 min at 1780 × *g* at room temperature. Peptides were purified using reversed-phase Sep-Pak C18 cartridges (Waters, Milford, MA) and eluted off the Sep-Pak with 40% ACN with a subsequent step of removal of acetonitrile by 48 hours lyophilisation. In the triple SILAC experiments, lyophilised peptides were dissolved in 25 mM ammonium hydroxide (NH_4OH) and subsequently offline fractionated by High-pH (HpH) RP chromatography using a Phenomenex Jupiter® C12 4 μm Proteo 90Å, LC 250 × 4.6 mm, Ea column on an ÄKTA-FPLC (fast protein liquid chromatography) system (GE Healthcare), operating at 1 ml/min, as previously described. Buffer A was 25 mM NH_4OH and Buffer B was 25 mM NH_4OH in 90% ACN. Fractions were collected using a collector in a 96-deep well plate at 1-min intervals. Samples were initially loaded onto the column at 1 ml/min for 3 min, after which the fractionation gradient was as follows: 5% B to 30% B in 60 min, 30% B to 60% in 2 min and ramped to 70% B for 3 min. At this point, fraction collection was halted, and the gradient was held at 100% B for 5 min before being ramped back to 5% B, where the column was then washed. A total number of 56 fractions were collected and concatenated into 14 fractions that were further analyzed, as previously described (Batth et al., 2014). After lyophilisation, each fraction derived from either the standard SILAC or the triple SILAC experiment was dissolved in 250 μL of 1x Immuno-Affinity Purification Buffer (IAP Buffer, #9993, Cell Signaling Technologies) and subjected to two consecutive steps of methyl-R peptides enrichment using the ADMA antibody-conjugated beads PTMScan Asymmetric Di-Methyl Arginine Motif [adme-R] Kit #13474, Cell Signaling Technologies) and MMA antibody-conjugated beads (PTMScan Mono-Methyl Arginine Motif [mme-RG] Kit #12235, Cell Signaling Technologies) following the manufacturer's instruction. After peptides incubation with the antibody-conjugated beads for 2 hours at 4°C, the immunoprecipitates were washed twice in ice-cold IAP Buffer, followed by three washes in water; then, bound methyl peptides were eluted with 2 × 50 μL 0.15% TFA. Peptide eluates were desalted on RP C18 StageTip microcolumns, as described previously (Rappsilber et al., 2007) and subjected to a second round of trypsin digestion prior to LC-MS/MS analysis.

Nano-LC-MS/MS analysis

Peptide mixtures were analyzed by online nano-flow liquid chromatography tandem mass spectrometry using an EASY-nLC 1000 (Thermo Fisher Scientific, Odense, Denmark) connected to a Q-Exactive instrument (Thermo Fisher Scientific) through a nano-electrospray ion source. The nano-LC system was operated in one column set-up with a 50-cm analytical column (75-μm inner diameter, 350-μm outer diameter) packed with C18 resin (EasySpray PEPMAP RSLC C18 2M 50 cm x 75 M, Thermo Fisher Scientific) configuration. Solvent A was 0.1% formic acid (FA) and solvent B was 0.1% FA in 80% ACN. Samples were injected in an aqueous 0.1% TFA solution at a flow rate of 500 nL/min. SILAC and hmSILAC immuno-enriched methyl peptides were separated with a gradient of 5%–40% solvent B over 90 min followed by a gradient of 40%–60% for 10 min and 60%–80% over 5 min at a flow rate of 250 nL/min in the EASY-nLC 1000 system. Label-free peptides from PRMT1 immunoprecipitation were analyzed in technical triplicates using a top-15 method with a linear 90 min gradient from 5 to 30% of solvent B, a MS1 resolution of 60,000 at m/z 400 and an accumulation time of 80msec for MS/MS.

The Q-Exactive was operated in the data-dependent mode (DDA) to automatically switch between full scan MS and MSMS acquisition. Survey full scan MS spectra (from m/z 300-1150) were analyzed in the Orbitrap detector with resolution R = 35,000 at m/z 400. The ten most intense peptide ions with charge states $\geq$ 2 were sequentially isolated to a target value of 3e6 and fragmented by Higher Energy Collision Dissociation (HCD) with a normalized collision energy setting of 25%. The maximum allowed ion accumulation times were 20ms for full scans and 50ms for MSMS and the target value for MSMS was set to 1e6. The dynamic exclusion time was set to 20 s.

Data analysis of the PRMT1 interactome

Protein interactors from the PRMT1 co-IP and PRMT1 X-ChroP were identified and quantified using MaxQuant software v.1.5.2.8. using the Andromeda search engine (Cox and Mann, 2008; Cox et al., 2011). In MaxQuant, the estimated false discovery rate (FDR) of all peptide identifications was set to a maximum of 1%. The main search was performed with a mass tolerance of 6 ppm. Enzyme specificity was set to Trypsin/P. A maximum of 3 missed cleavages was permitted, and the minimum peptide length was fixed at 7 amino acids. Carbamidomethylation of Cysteine was set as a fixed modification. The 2016 version of the Uniprot sequence was used for peptide identification.

Proteins identified both in the PRMT1 co-IP / X-ChroP experiments and in the corresponding negative controls (competition by specific blocking peptide and IgG, respectively) were profiled by quantitative label-free analysis, activating the label-free software MaxLFQ (Cox et al., 2014) as well as the "match between runs" feature. The "protein groups" MaxQuant output file was analyzed

using Perseus (Tyanova et al., 2016), plotting the LFQ values in a volcano plot graph, where the proteins enriched in the PRMT1 immunoprecipitations were compared to the negative controls. p values were calculated by Perseus using a two-tailed t test. For each protein, the variance of the LFQ quantitation in the 3 PRMT1 IPs and in the 3 control IPs was comparable. One missing value out of three replicates in each experimental group was allowed. Threshold setting for differential protein expression were S0 = 0.4, FDR = 0.01 for the comparison between PRMT1 co-IP in presence and absence of the blocking peptide. The PRMT1 interaction network was generated with experimentally validated protein-protein interactions from the STRING database (Snel et al., 2000) and visualized using Cytoscape 3.0 (Su et al., 2014).

Data analysis of arginine methyl peptides (SILAC and hmSILAC)

Acquired raw data were analyzed using the integrated MaxQuant software v1.6.2.10, using the Andromeda search engine (Cox and Mann, 2008; Cox et al., 2011). In MaxQuant, the estimated false discovery rate (FDR) of all peptide identifications was set to a maximum of 1%. The main search was performed with a mass tolerance of 6 ppm. Enzyme specificity was set to Trypsin/P. A maximum of 3 missed cleavages was permitted, and the minimum peptide length was fixed at 6 amino acids. Carbamidomethylation of Cysteine was set as a fixed modification. The September 2018 (2018_07) version of the Uniprot sequence database was used for peptide identification.

To assign and quantify SILAC methyl peptides, N-terminal acetylation, Methionine oxidation, mono-methyl-K/R, di-methyl-K/R were set as variable modifications.

The MaxQuant evidence.txt file was first filtered: potential contaminants and reverse sequences were removed; methyl peptides were required to have an Andromeda score > 25 and individual modifications were required to have a Localization Probability > 0.75. For the methyl peptides quantified more than once, the median SILAC ratio was calculated. Then, methyl peptide SILAC ratios were normalized on the respective protein SILAC ratios, calculated using unmodified peptides in the ''input'' experiment. To define significantly up- or downregulated methyl peptides by CDDP, we used mean (μ) and standard deviation (σ) based on the distribution of the unmodified peptide SILAC ratios calculated separately in the forward and reverse experiments and we applied a $\mu \pm 1\sigma$ cut-off to the distributions of the modified peptides of the respective replicate. These distributions were normal.

To assign hmSILAC peptide sequences, we defined new modifications in MaxQuant with the mass increment and residue specificities corresponding to heavy mono-methylation (mono-methyl4-K/R) and di-methylation (di-methyl4-K/R). Additionally, we defined new modifications for heavy Methionine (Met4) and oxidized heavy Methionine (OxMet4). To reduce the search complexity, raw data were analyzed twice with the following sets of variable modifications: (1) N-terminal acetylation, Met4, OxMet4, oxidation, mono-methyl-K/R, mono-methyl4-K/R; (2) N-terminal acetylation, Met4, OxMet4, oxidation, di-methyl-K/R, di-methyl4-K/R.

Identification of high confidence methyl sites was carried out with the Perl-based pipeline hmSEEKER (Massignani et al., 2019). To increase the confidence of our findings, we used hmSEEKER to automatically remove from our data any peptide with Andromeda score less than 25, Andromeda delta score less than 12 and/or carrying a modification with a localization probability less than 0.75. Heavy and light methyl-peptide pairs were considered true positive when the difference between calculated and expected mass shift was < 2 ppm and their retention time difference was < 30 s.

Validation of the methylated peptide identified in the SILAC experiments through the hmSILAC identifications was achieved by using a second bioinformatics tool developed *in house* (hmLINKER), which compares the sequences of the peptides in the SILAC dataset to those in the hmSILAC dataset. If a match is not immediately found at the sequence level, the peptide is not discarded, but a second round of match-attempt is performed at the individual modification sites level, using a window sequence.

Clustering and motif analysis of R-methyl peptides

Unsupervised clustering of methyl peptides was based on the distinct patterns of response to CDDP and PRMT1 knockdown (i.e., M/L, H/L, H/M SILAC ratios, in the forward and reverse experiment) and performed with the 'NbClust' R package using ''ward.D'' as clustering method.

Motif analysis of R methyl sites was performed using the iceLogo web application (Maddelein et al., 2015), which allows the visualization of significant enrichment variations between a reference set of sequences and a background set. In this work, the sequence windows centered on each methyl site were compared to a background composed of all methyl sites annotated in PhosphoSite Plus (Hornbeck et al., 2015). *P*-value threshold was set to 0.05.

Immunofluorescence analysis

Cells were plated on glass coverslips for 24 hours, fixed in 4% paraformaldehyde for 20 min at room temperature and permeabilized with 0.1% Triton X-100 in PBS for 2 min on ice. Then cells were incubated at RT with 2% BSA in PBS for 30 min and then with the anti-p65 C20 antibody (1:250) in PBS containing 2% BSA for 2 hours at room temperature. After being washed, cells were stained with Rabbit Alexa Fluor 488 secondary antibody (Molecular Probes, Eugene, OR, USA) diluted 1:400 diluted 1:100, in PBS containing 2% BSA for 1 hour at room temperature. Nuclei were stained with 4′,6-diamidino-2-phenylindole (DAPI). Images were obtained with a Leica TCS SP2 or Olympus IX71 (Leica Microsystems, Heerbrugg, Switzerland). For the IF analysis, the fields of the coverslips used for the quantification were randomly taken. Each field contained at least 50 cells and the quantification was performed using an *in-house* script which automatically calculates the intensity of the staining in the cytoplasm and nucleus of each cell. p65 was considered nuclear in the cells that display a p65 nuclear mean intensity/cytoplasm mean intensity $\geq$ 1.1.

RNA-seq analysis

RNA-seq was generated from Illumina platform. Data was aligned to human reference genome (GRCh37) using HISAT2 (Kim et al., 2015). Reference guided alignment was performed with GENCODE annotated transcripts. Differential analysis was performed on the basis of read counts using DESeq2 (Love et al., 2014). Genes with fold change of 4 and with adjusted *P*-value less than 0.05 are regarded as differentially regulated genes. Gene Ontology on differentially regulated genes was performed using DAVID (Huang da et al., 2009). All statistical analyses were performed using the R platform. The Mann-Whitney U test was used to test whether the differences between groups were significant or not.

RNA extraction, RT–PCR and qPCR

Total RNA was isolated from cells using Quick-RNA Miniprep kit (Zymo research), according to manufacturer's instructions. One μg of RNA from each sample was reverse-transcribed using ImProm-II Reverse Transcriptase (Promega) and random primers (Thermo Fisher Scientific), according to the manufacturer's protocol. Real-time quantitative PCR reactions were prepared using Fast SYBR™ Green reaction mix (Thermo Fisher Scientific) and performed on an Applied Biosystems 7500 Fast Real-time PCR system. The relative expression level was calculated with the $2^{[-\Delta\Delta Ct]}$ method and expressed as a "fold change": data were normalized to housekeeping gene (*GAPDH*) expression and compared to the untreated control. Primers used for profiling the mRNA expression levels of inflammatory related genes are as follows: *IL6* Fwd:5-CCAGAGCTGTGCAGATGAGT-3; Rev:5- ATTTGTGGTTGGGTCA GGGG-3; *IL1α* Fwd:5- AGGTTCTGAAGAAGAGACGGT −3; Rev:5- GGTGCTGACCTAGGCTTGAT-3; *IL1β* Fwd: 5- CTCTTCAGCCA ATCTTCATTGC-3; Rev: 5-GAACAAGTCATCCTCATTGCCA-3; *IL8* Fwd:5-CTTGGCAGCCTTCCTGATTTCT-3; Rev:5-GTTTTCCT TGGGGTCCAGACAG-3; *TNFα* Fwd:5-ACTTTGGAGTGATCGGCCC-3; Rev: 5- CATTGGCCAGGAGGGCATT-3.

Primers used for ChIP-qPCR analysis are the following: *IL6* promoter Fwd: 5-ATGTGGGATTTTCCCATGAGTC-3; Rev:5-GCCTCA GACATCTCCAGTCCTA-3; *IL8* promoter Fwd:5-TTGAAGCCCTCCTATTCCT-3; Rev:5- AAGGACTGACTATATAGCAG-3; *IL1A* promoter Fwd:5-ACTCCAACTGGGAACCCAAA-3; Rev:5-CTGTGGCCAGCCTAGTTCAG-3; *IL1B* promoter Fwd:5- GTGTCTTCCACT TTGTCCCACAT −3; Rev:5- TGACAATCGTTGTGCAGTTGATG-3; Negative control genomic region Fwd: 5-AGCTATCTGTCGAG CAGCCAAG-3; Negative control genomic region Rev: 5- CATTCCCCTCTGTTAGTGGAAGG-3.

Chromatin immunoprecipitation (ChIP) for DNA analysis

For the native ChIP, cells were harvested, washed twice with 1x PBS and pelleted. Cell pellets were re-suspended in 1 volume of Buffer B (15 mM NaCl, 15 mM Tris pH 7.6, 60 mM KCl, 2mM EDTA, 0.5mM EGTA, 0.3 M sucrose, 1 mM DTT, 0.5 mM PMSF, 0.2 mM spermine, 1 mM spermidine, H_2O as solvent) and then mixed with 1 volume of Lysis Buffer (15 mM NaCl, 15 mM Tris pH 7.6, 60 mM KCl, 2 mM EDTA, 0.5 mM EGTA, 1 mM DTT, 0.5 mM PMSF, 0.2 mM spermine, 1 mM spermidine, H_2O as solvent) and left 5 min on ice. Samples were then centrifuged at 1200 rpm for 5 min at 4°C and the nuclear pellets were washed with Buffer D (15 mM NaCl, 15 mM Tris pH 7.6, 60 mM KCl, 0.3 M Sucrose, 1 mM DTT, 0.5 mM PMSF, 0.2 mM spermine, 1 mM spermidine, H_2O as solvent). Nuclei were then resuspended in MNase Buffer (20mM Tris pH7.6, 5mM CaCl2, H_2O as solvent), counted, and the DNA was digested using as proportion of 1.5U MNase (Merck) for 3 nuclei. MNase digestion was performed for 90 minutes at 37°C in a thermomixer (700 rpm) and blocked afterward with 10 mM EDTA. The DNA was purified with the PCR purification kit (QIAGEN) and 2.5% of the material run on a 1% agarose gel, to verify that the DNA fragments were between 150-500 bp long. An aliquot (1%) of the MNase-digested nuclear extract was stored as input material, while the remaining part complemented with S300 Buffer (10 mM Tris pH7.6, 0.3M NaCl, 0.2% Igepal, H_2O as solvent) and left on ice for 20 min. Afterward, samples were centrifuged in a table-top centrifuge for 30 min at 10000 g in order to precipitate the cell debris, and the supernatant transferred into clean Eppendorf tubes and adjusted to a final volume of 1 mL with S300 buffer. The nuclear extract was then rocked overnight on a rotating wheel at 4°C with 10 ug of either anti-H4R3me2a Ab, or rabbit IgG as negative control. On the following day, 40 uL of slurry protein-G Sepharose beads (GE-Healthcare), pre-washed twice with S300 Buffer, were added to each sample and rocked for 3 hours on a rotating wheel at 4°C. At the end of the incubation, the immuno-complexes were washed five times in S300 Buffer and the DNA was eluted and purified using the PCR purification kit. The DNA of the input material was also extracted and purified using the same protocol. The DNA (2,5% of the total volume) was then analyzed by real time PCR for selected target genes.

The crosslinked ChIP experiments were, instead, performed according to the protocol previously described (Ferrari et al., 2014). Briefly, cells were harvested, washed twice with 1x PBS and crosslinked with 1% formaldehyde for 10 min at room temperature. The crosslinking process was stopped by addition of 0.125 M glycine for 5 min at room temperature. Fixed cells were then washed twice with PBS, lysed in SDS Buffer (50 mM Tris at pH 8.1, 0.5% SDS, 100 mM NaCl, 5 mM EDTA, and protease inhibitors) and sonicated to sheared the chromatin to ~500 bp. An aliquot of the sample (2.5%) was purified with the PCR purification kit (QIAGEN) and the isolated DNA run on a 1% agarose gel, to verify that the DNA fragments were around 500 bp long. The sonicated lysates were then diluted with IP Buffer (33 mM Tris-HCl pH 8, 100 mM NaCl, 5 mM EDTA, 0.2% NaN3, 0.33% SDS, 1.66% Triton X-100) to bring all samples to the same final concentration and an aliquot of input material (5%) was taken. Samples were then incubated with 5 ug of either rabbit IgG (Millipore) or p65 antibody (Cell Signaling) overnight at 4°C. The following day, samples were incubated for 3 hours with protein-G Sepharose beads (GE Healthcare) and at the end of the incubation, beads were washed 3 times with low-salt Buffer (150 mM NaCl, 20 mM Tris-HCl pH 8, 2 mM EDTA, 0.1% SDS, 1% Triton X-100) and once with high-salt Buffer (500 mM NaCl, 20 mM Tris-HCl pH 8, 2 mM EDTA, 0.1% SDS, 1% Triton X-100). Finally, beads were re-suspended in de-crosslinking solution (0.1 M NaHCO3, 1% SDS) and left at 65°C for 2h to decrosslinked the DNA and elute it from the beads. The DNA was

subsequently purified with QIAquick PCR purification kit (QIAGEN) according to manufacturer's instructions. The DNA (2,5% of the total volume) was then analyzed by real time PCR for selected target genes.

Multiplexed immuno-based assay for cytokine quantification

Protein levels of IL6, IL8 and TNFα inflammatory cytokines in the supernatant of SK-OV-3 cells after 36 hours of CDDP treatment (20 μM), with and without the pre-treatment with 5 μM MS023 were quantified using the Bead-based immunoassays, according to the manufacturer's instructions (CBA, BD BioSciences, 170116). Statistical analysis of the data was performed using ANOVA (Microsoft Excel; Microsoft, Redmond, WA, USA). Four technical replicates (n = 4) were carried out.

Clonogenic assay

Cells were harvested, washed twice with ice-cold 1x PBS and fixed with ice-cold methanol for 10 min. Afterward, 1% crystal violet solution (Sigma V5265) was added to the plates and incubated at room temperature for 10 min. Plates were then washed with distilled H_2O, until the unbound crystal violet was removed and plates were dried at room temperature. For the clonogenic assay, images were acquired with ScanR and colonies counted using the ImageJ plugin ''analyse particles.'' Statistics analysis were performed using the t test and values were considered significative when the *P*-value was < 0.05. Biological replicates n = 4.

Apoptosis assay

Control and PRMT1-depleted SK-OV-3 cells were grown for 72 hours in the presence or absence of 20 μM CDDP and apoptosis was measured by means of APC-conjugated Annexin V (Thermo Fisher Scientific) and propidium iodide (Thermo Fisher Scientific), in accordance with the manufacturer's instructions. The samples were acquired using the FACSCalibur platform (BD Bioscience) and analyzed using the FlowJo software. Statistical analysis was performed using ANOVA (Microsoft Excel; Microsoft, Redmond, WA, USA). Statistics analysis included in the Apoptosis assay were performed on samples which were normally distributed and showing the same variance by applying the Two-Factor Without Replication -ANOVA test. Biological replicates n = 3.

QUANTIFICATION AND STATISTICAL ANALYSIS

All quantitative data were collected from experiments performed in biological replicates and expressed as mean ± standard deviation (SD) as indicated in the figure legends. When biological replicates n = 2, the standard deviation is indicated as variation in the figure legend. Differences between groups were assayed with the statistical test indicated in the respective figure legend using Microsoft Excel, Perseus or R-platform. Significant differences were considered when *P*-value ≤ 0.05.

Volcano Plot analysis

Label-free quantitative (LFQ) values derived from at least 3 biological replicates analyzed by MaxQuant were plotted with either Perseus or R-platform in a volcano plot graph and *P*-values calculated using a two-tailed t test.

RNA-seq analysis

Genes with fold change of 4 and with adjusted *P*-value less than 0.05 were considered as differentially regulated genes. Statistical analyses were performed using the R-platform. The Mann-Whitney U test was used to test whether the differences between groups were significant or not.

Western Blot quantification

The quantification of the Western Blot images was done using Fiji (Schindelin et al., 2012).

DATA AND CODE AVAILABILITY

The accession number for the RNA-seq data reported in this paper is GEO Database: GSE106609.

The accession number for the MS-proteomics data reported in this paper is ProteomeXchange Database: PXD014799.

Perl codes used to process the SILAC data and to intersect it with the hmSEEKER output are available upon request.